



Comparative analysis of the anticorrosive properties of trivalent chromium conversion coatings formed on 2024-T3 and 2024-T351 aluminium alloys

Xavier Verdalet-Guardiola, Romain Saillard, Benoit Fori, Sandrine Duluard, Christine Blanc

► To cite this version:

Xavier Verdalet-Guardiola, Romain Saillard, Benoit Fori, Sandrine Duluard, Christine Blanc. Comparative analysis of the anticorrosive properties of trivalent chromium conversion coatings formed on 2024-T3 and 2024-T351 aluminium alloys. Corrosion Science, 2020, 167, pp.108508. 10.1016/J.CORSCI.2020.108508 . hal-03165264

HAL Id: hal-03165264

<https://hal.science/hal-03165264>

Submitted on 10 Mar 2021

HAL is a multi-disciplinary open access archive for the deposit and dissemination of scientific research documents, whether they are published or not. The documents may come from teaching and research institutions in France or abroad, or from public or private research centers.

L'archive ouverte pluridisciplinaire **HAL**, est destinée au dépôt et à la diffusion de documents scientifiques de niveau recherche, publiés ou non, émanant des établissements d'enseignement et de recherche français ou étrangers, des laboratoires publics ou privés.



Open Archive Toulouse Archive Ouverte

OATAO is an open access repository that collects the work of Toulouse researchers and makes it freely available over the web where possible

This is an author's version published in:

<http://oatao.univ-toulouse.fr/26642>

Official URL

DOI : <https://doi.org/10.1016/J.CORSCI.2020.108508>

To cite this version: Verdalet-Guardiola, Xavier and Saillard, Romain and Fori, Benoit and Duluard, Sandrine and Blanc, Christine *Comparative analysis of the anticorrosive properties of trivalent chromium conversion coatings formed on 2024-T3 and 2024-T351 aluminium alloys.* (2020) Corrosion Science, 167. 108508. ISSN 0010938X

Any correspondence concerning this service should be sent to the repository administrator: tech-oatao@listes-diff.inp-toulouse.fr

Comparative analysis of the anticorrosive properties of trivalent chromium conversion coatings formed on 2024-T3 and 2024-T351 aluminium alloys

X. Verdalet-Guardiola^{a,b,c}, R. Saillard^a, B. Fori^c, S. Duluard^b, C. Blanc^{a,*}

^a CIRIMAT, Université de Toulouse, CNRS, INP ENSIACET, 4 allée Emile Monso, BP 44362, 31030, Toulouse Cedex 4, France

^b CIRIMAT, Université de Toulouse, CNRS, UPS, 118 route de Narbonne, 31062, Toulouse Cedex 9, France

^c MECAPROTEC Industries, 34 Boulevard de Joffrey, BP 30204, 31605, Muret Cedex, France

ABSTRACT

Keywords:

A. Aluminium

A. Copper

A. Intermetallics

B. EIS

B. Polarisation

C. Oxide coatings

The anticorrosive properties of the trivalent chromium process (TCP) coatings were studied for a 2024 aluminium alloy (AA2024) in both T3 and T351 metallurgical states. Better corrosion resistance was measured for the TCP coated AA2024-T3 compared to AA2024-T351, which was clearly related to the surface copper coverage measured after the pre-treatments for the different samples. The differences were explained considering the reactivity of both the S-phase coarse intermetallics (IMCs) and intergranular Cu-rich precipitates during deoxidation. Large S-phase IMCs and numerous intergranular Cu-rich precipitates constituted critical metallurgical parameters for the anticorrosive properties of the TCP coatings.

1. Introduction

Al alloys are widely used in the aeronautical industry because they allow a decrease of the structure mass due to their good mechanical properties, e.g. high specific modulus, obtained by the addition of alloying elements [1]. However, this is associated with a heterogeneous microstructure, and consequently with a susceptibility to localised corrosion [2–4]. Hence, Al alloys cannot be used without an anticorrosive treatment. Hexavalent Cr conversion coatings are largely used to protect Al alloys against corrosion, but they will be banned from use in 2024 in the aeronautic field by the European regulation REACH [5]. Therefore, a lot of research studies have been focused on the development of Cr(VI)-free conversion coatings, e.g. trivalent Cr process (TCP) coatings [6–10]. TCP is used in particular for the 2024 Al alloy (AA2024). AA2024 has been used for more than 30 years in the aeronautic industry, because it exhibits good mechanical properties and fatigue resistance; however, it also has a low corrosion resistance associated, as said above, with a heterogeneous microstructure [11]. For a T3 thermomechanical treatment, the quenching, following the solution heat treatment, does not allow the precipitation of S''/S' (Al₂CuMg type) or θ''/θ' (Al₂Cu type) hardening precipitates. Therefore, AA2024-T3 exhibits only a Cu-supersaturated solid solution in which Guinier-Preston and/or Guinier-Preston-Bagaryatsky zones can be distinguished [12,13]. Slower cooling of the alloy, which can occur at the core of a thick plate, corresponding to a T351 thermomechanical treatment, can

allow the precipitation of hardening precipitates, but mainly that of intergranular precipitates [14]. Therefore, significant differences in microstructure are observed between AA2024-T3 and AA2024-T351. These microstructural differences can be associated with different anticorrosive properties of TCP coatings as shown by Saillard et al. [15]. Moreover, coarse intermetallic particles (IMCs) are formed during Al alloy casting and are not dissolved during the solution heat treatment, during which they can grow [16]. In AA2024, the most commonly observed IMCs are Al₂CuMg (S-phase) and Al-Cu-Mn-Fe particles with a wide range in composition [12]. Those particles are present in both T3 and T351 samples but have a smaller size in T3 sample [15,17]. Such a difference in IMCs size can be linked to the differences in the thermomechanical treatment, taking into account that a mechanical treatment, e.g. rolling, can lead to the fragmentation of IMCs, and therefore reduces their diameter [18,19]. The electrochemical behaviour of S-phase has been widely studied, and it is well known that its dissolution can lead to Cu redeposition [10,15,20]. Moreover, the detrimental effect of Cu enrichment on TCP coating anticorrosive properties has been shown by many authors [15,21,22]. Therefore, considering all the microstructural differences that exist between AA2024-T3 and AA2024-T351, it could be expected significant differences in the anticorrosive properties of the TCP coatings formed on both alloys. This topic is of major interest, in particular from an industrial point of view, because the certification of the surface treatments for AA2024 is commonly performed by using AA2024-T3 only.

* Corresponding author.

E-mail address: christine.blanc@ensiacet.fr (C. Blanc).

Therefore, in the present paper, the anticorrosive properties of the TCP coatings formed on the surface of both AA2024-T3 and AA2024-T351 alloys were compared by using neutral salt spray tests (NSS), polarisation curves and electrochemical impedance spectroscopy (EIS). Then, to explain the results, cyclic voltammetry (CV) was used to measure the surface Cu coverage after the pre-treatment step; finally, scanning and transmission electron microscope (SEM and TEM) observations were performed to identify the critical microstructural parameters, which contributed to explain the anticorrosive properties of the TCP coatings formed on both AA2024-T3 and AA2024-T351 alloys.

2. Materials and methods

2.1. Materials and sample preparation

Samples were machined from a 3-mm thick sheet and a 60-mm thick plate of AA2024, all provided by Constellium. The 3-mm thick sheet and the 60-mm thick plate were in the T3 and T351 metallurgical states, respectively. Both metallurgical states corresponded to rolling, solution heat treatment, water quenching, stress relieve and natural ageing at room temperature. The difference between the two metallurgical states was that T3 corresponded to hot and cold rolling, whereas only hot rolling was achieved for the T351 state, leading to a thicker plate. Samples from the 3-mm thick sheet and from the 60-mm thick plate are referred as AA2024-T3 and AA2024-T351, respectively. Chemical composition of the alloys are reported in Table 1. It could be noted here that the Cu content of the two alloys was quite similar (4.4 wt. % for AA2024-T3 and 4.2 wt. % for AA2024-T351). Verdalet et al. [10] showed, for samples of AA2024-T3 machined from two sheets of similar composition (4.5 wt. % and 4.4 wt. %, i.e. with differences in Cu content in the same range as observed in the present study), that no significant differences in anticorrosive properties of the TCP coating could be measured. Therefore, it was relevant to consider here that the results concerning the anticorrosive properties of the TCP coatings formed on AA2024-T3 and AA2024-T351 could not be explained by considering such a small difference in Cu content. AA2024-T3 samples were $120 \times 80 \times 3 \text{ mm}^3$ parallelepipeds with the TCP coating grown on the longitudinal (i.e. rolling, L)/long transverse (LT) plane. Therefore, for AA2024-T3 alloy, only one plane of the sheet was studied, which was relevant taking into account the industrial application. For AA2024-T351 samples, some were machined with the main plane parallel to the L/LT plane of the plate for two sampling depths, i.e. in the core of the plate (30-mm depth), and on its surface (0-mm depth). Others were machined with their main plane parallel to the LT/ST (short transverse) plane of the plate. They were $120 \times 60 \times 3 \text{ mm}^3$ parallelepipeds. Before the pre-treatments, all samples were abraded using SiC papers down to P-grade 2400 and then polished with a 1 μm diamond paste.

TCP treatment was performed using a multi-step process. Industrial grade chemical reactants were used for all solutions, and the samples were rinsed in deionised water after each step. Due to confidentiality reasons, the exact composition of the solutions cannot be given. Firstly, samples were rinsed with acetone in order to remove surface pollutants. Then, they were immersed in a degreaser alkaline bath (40 g L^{-1} sodium tripolyphosphate, 40 g L^{-1} borax and 5 mL L^{-1} Turco 4215 additive, $\text{pH} = 9$) at 60°C for 1200s. The following deoxidation step was used to remove IMCs and the native oxide. For this step, two solutions

were tested in order to show that differences in anticorrosive properties of the TCP coatings formed on AA2024-T3 and AA2024-T351 were observed independently of the pre-treatment. Both solutions were a sulfo-nitro-ferric solution, but with differences in their composition. The first solution was a Socosurf A1858-A1806 ($\text{pH} < 1$) provided by Socomore (France) and called deoxidation 1; samples were immersed in this solution at 50°C for 300 s, leading to a dissolution rate of about 50 nm min^{-1} . For the second solution ($\text{pH} = 1$), called deoxidation 2, samples were immersed at room temperature for 300 s, leading to a dissolution rate of about 0.2 nm min^{-1} . It is important to note here that, due to the differences in both concentration of the species present in the deoxidation solutions and temperature, differences in the surface chemistry after the pre-treatment, and consequently in the morphology and anticorrosive properties of the TCP coatings formed on a specific alloy, should be observed. But, no significant differences in chemistry of the TCP coatings were expected, and it was not the focus of this work to perform such a study. Finally, the TCP coating was formed by immersing the samples in a Zr/Cr-containing Socosurf TCS solution (32 %v/v Socosurf TCS (Socomore, France), $3.8 < \text{pH} < 4$) at 40°C for 600 s. This treatment was completed by a post-treatment, which corresponded to an immersion of the samples covered by the coating in the rare-earth element containing post-treatment PACS solution (10 % v/v Socosurf PACS provided by Socomore, France, 5 % v/v H_2O_2 at 35 % v/v in water, pH between 4.2 and 5.3) at room temperature for 300 s. Finally, samples were dried at 60°C during 600 s. For TCP coated samples, all tests were performed at least 48 h after the conversion treatment.

2.2. Electrochemical measurements

The electroactive Cu content on a 4-cm^2 sample surface, called surface Cu coverage (θ_{Cu}), was determined by cyclic voltammetry (CV) experiments as described in Scully's work [23,24]. A three-electrode cell connected to a Bio-Logic VSP potentiostat was used with a saturated calomel electrode (SCE) as reference electrode and a platinum electrode as counter electrode. Measurements were performed in a deaerated borate buffer solution ($8.17 \text{ g L}^{-1} \text{ Na}_2\text{B}_4\text{O}_7 - 10 \text{ H}_2\text{O}$, $7.07 \text{ g L}^{-1} \text{ H}_3\text{BO}_3$, $\text{pH} = 8.4$) at room temperature. Before CV, the solution was deaerated for 15 min with nitrogen bubbling. The measurement procedure consisted of three CV scans and could be described as follows: (a) polarisation at $-0.7 V_{\text{SCE}}$ during 5 min; (b) scan from $-0.7 V_{\text{SCE}}$ to $0.3 V_{\text{SCE}}$ then back to $-1.2 V_{\text{SCE}}$ at 1 mV s^{-1} ; (c) hold at $-0.7 V_{\text{SCE}}$ during 10 min; (d) repeat step (b); (e) hold at $-0.7 V_{\text{SCE}}$ during 20 min; (f) repeat step (b). During the first two cycles, the signal corresponding to Al oxidation was reduced (due to the polarisation at $-0.7 V_{\text{SCE}}$ and nitrogen bubbling), allowing the Cu peak to be clearly observed. Therefore, the electroactive Cu content was determined by measuring the area under the $\text{Cu(0)} \rightarrow \text{Cu(I)}$ peak in the last scan, by using Eq. (1):

$$\theta_{\text{Cu}} (\%) = \frac{\text{Area under Cu(0) to Cu(I) peak of studied samples}}{\text{Area under Cu(0) to Cu(I) peak of pure copper}} \times 100 \quad (1)$$

In the following, the surface Cu coverage values are calculated from at least three experiments. As shown by this equation, pure Cu was a reference; therefore CV experiments were first performed on pure Cu. Two oxidation peaks were identified: the first peak corresponded to the oxidation of Cu (0) to Cu (I), and the second one to the oxidation of Cu (I) to Cu (II). To avoid errors on the measurements, only the first peak

Table 1
Chemical composition of AA2024-T3 and AA2024-T351 samples.

El. (wt. %)	Al	Cu	Mg	Mn	Fe	Si	Zn	Ti	Cr	Zr	Ni
AA2024-T3	Base	4.4	1.4	0.51	0.15	0.08	0.17	0.02	0.01	0.01	54 ppm
AA2024-T351		4.2	1.4	0.51	0.15	0.09	0.18	0.03	0.01	0.01	66 ppm

was analysed because it was more intense than the second one. CV scans for pure Cu can be seen in our previous work [15].

The corrosion properties of the TCP coated samples were first evaluated by neutral salt spray tests (NSST) because these tests are widely used in industry and defined by the ISO9227 standard. In addition, the aeronautical standard requires NSST in order to certify conversion layers. In this framework, NSST results were relevant and helpful in strengthening the industrial impact of the results. Exposure of the samples was achieved in an Ascott salt spray chamber S120iS under ISO9227 standard. Parallelepiped samples were used with a 1-dm² surface area; they were inspected each 24 h and the number of pits was determined. From an industrial point of view, when the number of pits was equal or higher than 5, the corrosion was considered as general corrosion. For reproducibility reason, two or three tests were performed for each condition. In the conditions of the test, corrosivity tests for CR4 steel exhibited a corrosion rate of 68 g m⁻² for 48 h.

Then, to complete these results and to provide a more accurate analysis of the anticorrosive properties of the TCP coatings, both polarisation tests and electrochemical impedance spectroscopy (EIS) experiments were performed in a 0.5 M NaCl solution. As for surface Cu coverage measurements, a three-electrode cell connected to a Bio-Logic VSP potentiostat was used. The working electrode was a parallelepiped sample, with the studied surface being placed horizontally at the bottom of the cell. The saturated calomel electrode (SCE), used as reference electrode, and the graphite rod electrode, used as counter electrode, were placed above at a distance of about 10 mm. Preliminary experiments were also performed with the working electrode placed vertically in the cell in order to check whether possible phenomenon of corrosion products deposition could disturb the measurements. No significant differences were observed between the two configurations (commented in the discussion part), and the conclusions were exactly the same for both cell configurations. Moreover, preliminary open circuit potential (OCP) measurements were performed for all samples: results showed that, for all samples, OCP values decreased abruptly during the first 5 min, then progressively increased and remained stable after 30 min. Therefore, samples were maintained at their OCP for 1 h, and then the anodic and cathodic curves (surface exposed of 4 cm²) were obtained independently, with a potential sweep rate of 0.14 mV s⁻¹. With these experimental conditions, the corrosion potential measured on the polarisation curves was equal to the stable OCP value measured after 1 h. For EIS experiments, a 10-cm² sample surface was first exposed to the solution for 1 h at OCP before EIS measurements, as for polarisation tests. Then, EIS measurements were performed at the OCP in the frequency range 1 10⁵ to 1 10⁻² Hz with a potential amplitude (rms) of 10 mV, for different immersion times until 21 days. For brevity, only the results obtained for a 21-day immersion are given in the following. All electrochemical tests were performed at least three times for reproducibility. All values given in the discussion part are mean values calculated from those repeated measurements.

2.3. Morphological characterisations

The surface morphology of the TCP coatings was observed by using a scanning electron microscope (SEM) with a Field Emission Gun (SEM-FEG), JEOL JSM 6100 F (platform of micro-characterisation Raimond Castaing, Toulouse, France). The SEM-FEG operated at 5 kV in secondary electrons mode. Cross-sections were realised with a SEM-Focused Ion Beam (SEM-FIB) FEI HELIOS 600i equipped with a gallium Ionic Canon (platform of Micro-characterisation Raimond Castaing, Toulouse, France). Gallium canon operated at 30 kV and 47 nA to 80 pA during cutting. Before cutting, samples were gold-plated, then covered by an electronic carbon layer (thickness 0.5 µm, voltage 5 kV and probe current 2.5 nA, precursor: naphthalene (C₁₀H₈)) and a 3 µm thick ionic platinum layer (voltage 30 kV and probe current 0.43 nA, precursor: methylcyclopentadieny(trimethyl)platinum (C₅H₄CH₃Pt(CH₃)₃)). Energy dispersive X-ray spectroscopy (EDS) analyses were performed

by using an EDX Aztec Advanced (Oxford Instruments) with SDD X-Max 80 mm² detector. To complete the analyses, the samples were also observed by transmission electron microscopy (TEM, JEOL JEM 2100 F, platform of micro-characterisation Raimond Castaing, Toulouse, France) operating at 200 kV, and combined with EDS analyses (SDD Bruker). Finally, glow-discharge optical emission spectroscopy (GD-OES) analyses were also performed by using a HORIBA Jobin Yvon GD-Profilier 2 (platform of micro-characterisation Raimond Castaing, Toulouse, France), operating with an argon pressure of 630 Pa, a power of 30 W, radiofrequency of 13.56 MHz, with a 4-mm diameter copper anode. Before sampling, a flush time of 120 s was operated. Instability of the plasma initiation was avoided by covering the samples by a gold sputtered layer. An acquisition interval of 0.01 s was fixed. The emission lines used here were Al 396.152 nm, Cu 324.754 nm, Zr 339.198 nm, Cr 425.433 nm and Au 242.795 nm.

3. Results

3.1. Corrosion behaviour of TCP coated AA2024 samples

Firstly, the corrosion behaviour of the TCP coated AA2024 alloys was evaluated by using NSST. The number of pits observed for AA2024-T3 and AA2024-T351 during NSST are reported in Fig. 1. Results show that TCP coated AA2024-T3 and AA2024-T351, pre-treated with deoxidation 1, exhibit significant differences in corrosion resistance (Fig. 1a and b). The first pit appeared after 144 h in the NSST chamber for AA2024-T3 (L/LT), whereas it appeared after only 48 h for AA2024-T351 (L/LT_{core}) (Fig. 1a). Moreover, results obtained after NSST exposure for different planes of the AA2024-T351 plate (Fig. 1b) showed that, independent of the plane, the first pit appeared after 48 h and general corrosion between 48 and 72 h of NSST exposure. This showed similar anticorrosive properties of the TCP coating formed on the AA2024-T351 plate, independently of the plane, and better corrosion behaviour for the TCP coated AA2024-T3 sheet than for the TCP coated AA2024-T351 plate. To check that such differences were not specific of deoxidation 1 solution, results from NSST exposure of TCP coated AA2024-T3 (L/LT) and AA2024-T351 samples (LT/ST), pre-treated with deoxidation 2, are given in Fig. 1c; results obtained for a pre-treatment with deoxidation 1 are reported for comparison. For AA2024-T3 samples, the first pit appeared after 300 h with deoxidation 2, whereas the first pit occurred rapidly (24 h or less) after the beginning of the NSST exposure for AA2024-T351 samples. Therefore, results clearly showed that the TCP coated AA2024-T3 exhibited better corrosion behaviour than TCP coated AA2024-T351, after both deoxidation 1 and deoxidation 2 pre-treatments. It was interesting to note that deoxidation 1 solution led to a lower corrosion resistance of AA2024-T3 samples after TCP treatment as compared to deoxidation 2 solution. For AA2024-T351, due to the low anticorrosive properties of the TCP coatings formed, the NSST did not allow to evaluate the influence of the deoxidation solution on those properties.

To go further in the characterisation of the anticorrosive properties of the TCP coatings, potentiodynamic polarisation and EIS measurements were performed (Fig. 2). Polarisation curves plotted in a 0.5 M NaCl solution for both TCP coated AA2024-T3 and AA2024-T351 samples, with a pre-treatment corresponding to deoxidation 1, are reported in Fig. 2a. All samples exhibited a similar corrosion potential around -0.73 ± 0.02 V_{SCE}. Moreover, the global shape of the polarisation curves was similar for all samples with a passivity plateau observed in the anodic domain, which was characteristic of the electrochemical answer of the TCP coating. In a 0.5 M NaCl solution, bare metals were susceptible to localised corrosion at their corrosion potential, and a sharp increase of the anodic current densities was observed at the corrosion potential (results not shown). An accurate analysis of the curves allowed to distinguish between two types of corrosion behaviour. Firstly, AA2024-T3 and the L/LT_{surface} plane of AA2024-T351 had a similar corrosion behaviour with a well-defined passivity plateau,

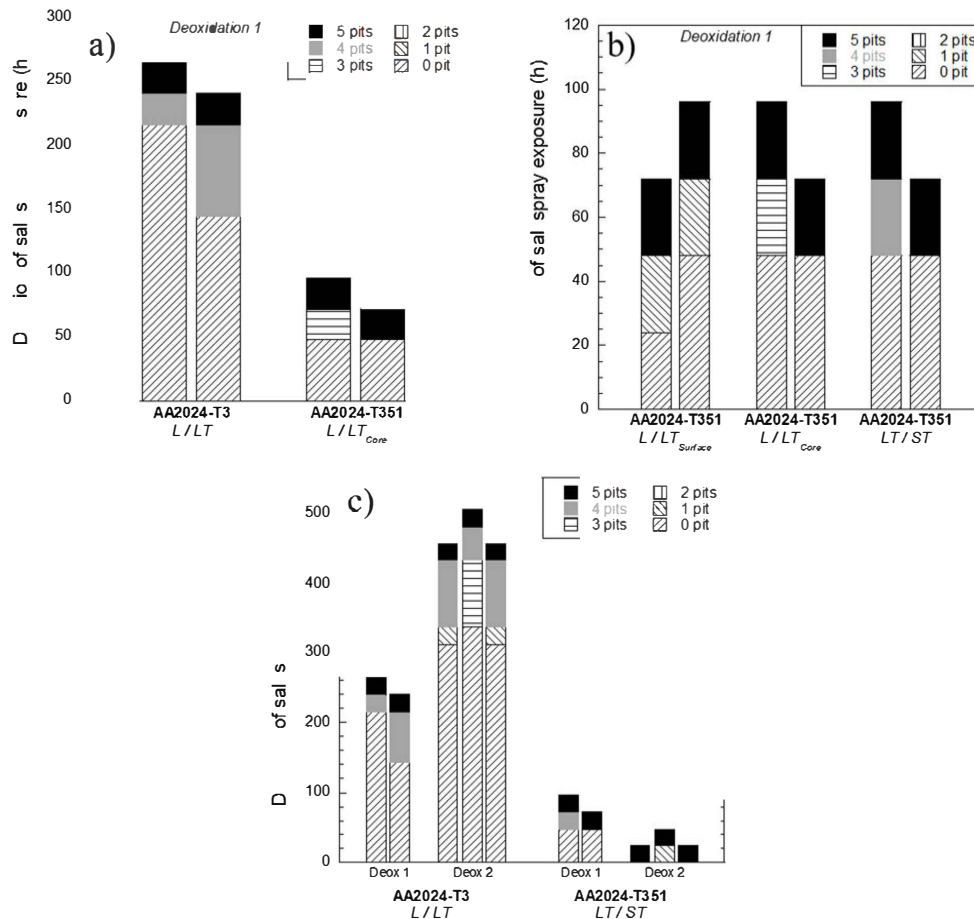


Fig. 1. Neutral Salt Spray Test results obtained for a) TCP coated AA2024-T3 (L/LT) and AA2024-T351 (L-LT_{core}) deoxidised with deoxidation 1 solution), b) TCP coated AA2024-T351 (L/LT_{surface}, L/LT_{core} and LT/ST) deoxidised with deoxidation 1 solution) and c) TCP coated AA2024-T3 (L/LT) and AA2024-T351 (LT/ST) deoxidised with deoxidation 1 and deoxidation 2 solutions.

even though a weak positive slope could be observed on the passivity plateau, which was more marked for the L/LT_{surface} plane of AA2024-T351; this could be linked to the aggressivity of the 0.5 M NaCl solution. Considering that the corrosion behaviour was controlled by the presence of the TCP coating, the corrosion current was calculated by extrapolation of the passivity plateau until the corrosion potential value. For samples for which the passivity plateau was not so well-defined, this procedure led to a lack of accuracy in the corrosion current density values, but the authors assumed that this procedure constituted a rather good estimation of this parameter. For both AA2024-T3 and the L/LT_{surface} plane of AA2024-T351, corrosion current densities were found to be equal to $8.1 \pm 0.5 \cdot 10^{-9} \text{ A cm}^{-2}$. However, a slightly more positive pitting potential (determined by extrapolation of the passivity plateau and the part of the anodic branch corresponding to the sharp increase of the current density) was reported for AA2024-T3 ($-0.58 \pm 0.01 \text{ V}_{\text{SCE}}$) as compared to the L/LT_{surface} plane of AA2024-T351 ($-0.60 \pm 0.02 \text{ V}_{\text{SCE}}$); moreover, the anodic current densities on the passivity plateau were slightly higher for the L/LT_{surface} plane of AA2024-T351 as compared to AA2024-T3 ($2.0 \pm 0.6 \cdot 10^{-8} \text{ A cm}^{-2}$ and $4.2 \pm 0.5 \cdot 10^{-8} \text{ A cm}^{-2}$ for AA2024-T3 and L/LT_{surface} plane of AA2024-

T351, respectively for a potential of $-0.66 \text{ V}_{\text{SCE}}$. Those values were different from the corrosion current density values due to the slope noted in the passivity plateau). It is clear that the differences between the different values were weak. However, the experiments were reproduced five times and results were very reproducible. The values given corresponded here to the mean values from five experiments. Moreover, same conclusions were obtained with the working electrode placed in a vertical position. Nevertheless, considering the small amplitude of the differences, the only relevant conclusion was that the results showed a good resistance to pitting corrosion for the TCP coated AA2024-T3 and the TCP coated L/LT_{surface} plane of AA2024-T351, even though they also suggested that the L/LT_{surface} plane of AA2024-T351 was slightly more susceptible to pitting than AA2024-T3 samples. Then, results also showed that the L/LT_{core} and LT/ST planes of the AA2024-T351 plate did not exhibit similar properties compared to the L/LT_{surface} plane of AA2024-T351 and AA2024-T3 samples. Indeed, the corrosion current densities were higher ($1.9 \pm 0.4 \cdot 10^{-8} \text{ A cm}^{-2}$ and $4.1 \pm 0.6 \cdot 10^{-8} \text{ A cm}^{-2}$ for the L/LT_{core} and LT/ST planes of the AA2024-T351 plate, respectively) indicating a faster corrosion kinetics. Moreover, for both samples (L/LT_{core} and LT/ST planes of the AA2024-T351 plate), the

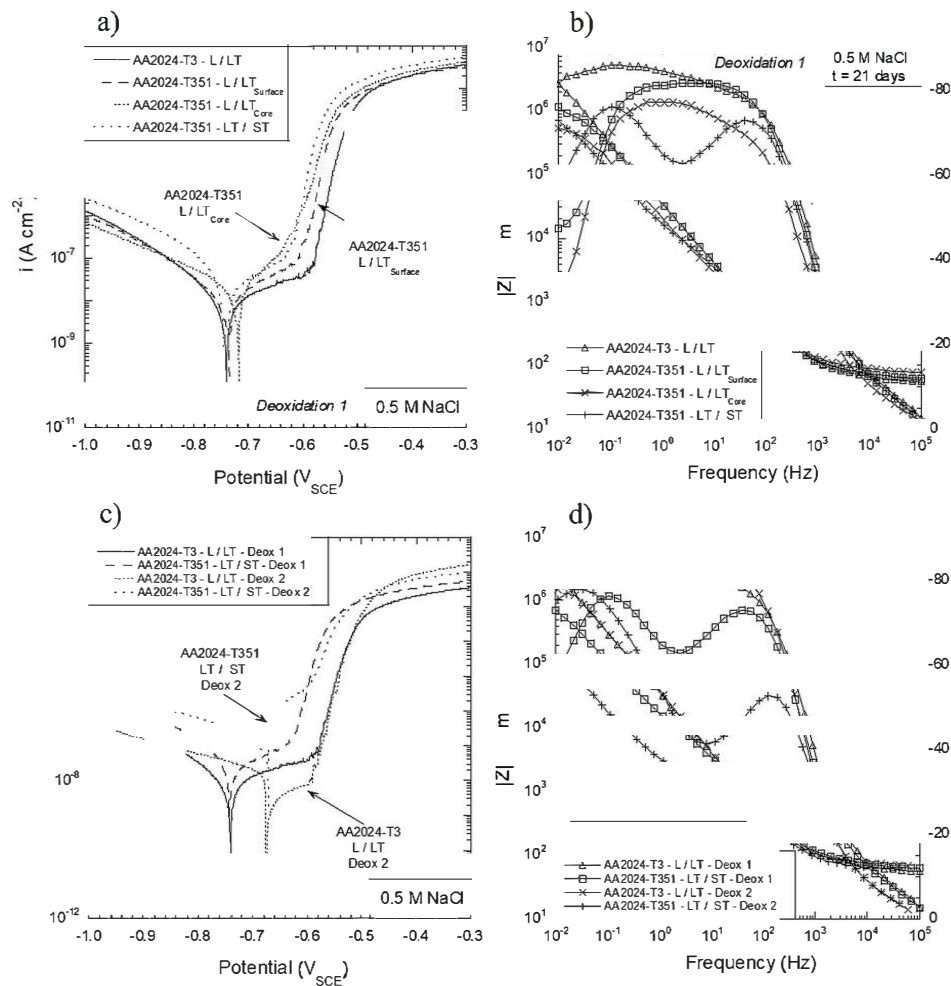


Fig. 2. a) Polarisation curves and b) impedance diagrams (at OCP, after 21 days of immersion) plotted for TCP coated AA2024-T3 (L/LT) and AA2024-T351 (L/LT_{surface}, L/LT_{core} and LT/ST) deoxidised with deoxidation 1 solution. c) Polarisation curves and d) impedance diagrams (at OCP, after 21 days of immersion) plotted for TCP coated AA2024-T3 (L/LT) and AA2024-T351 (LT/ST) deoxidised with deoxidation 1 and deoxidation 2 solutions. All measurements are performed in 0.5 M NaCl.

passivity plateau was not well-defined, which showed the aggressivity of the electrolyte towards those TCP coatings, and the anodic current densities were higher ($1.1 \pm 0.5 \cdot 10^{-7}$ A cm⁻² at -0.66 V_{SCE}) than for the two other samples. The pitting potential measured for L/LT_{core} and LT/ST planes of the AA2024-T351 plate was also more negative than for the two other samples, and equal to -0.63 ± 0.01 V_{SCE}. Here also, the differences were weak, but reproducible. Results obtained from experiments performed with working electrodes placed vertically in the cell did not show significant differences and led to the same conclusions. Therefore, the results showed better anticorrosive properties for the TCP coating formed on AA2024-T3 compared to AA2024-T351, as previously shown with NSST. Moreover, the polarisation curves allowed to distinguish between the anticorrosive properties of the TCP coatings formed on AA2024-T351 depending on the planes of the plate: results indicated lower anticorrosive properties for the TCP coatings formed on the L/LT_{core} and LT/ST planes of the AA2024-T351 plate as

compared to the L/LT_{surface} plane of the same plate. To complete those results, EIS spectra were plotted for different immersion times, from 1 h to 21 days, in 0.5 M NaCl for TCP coated AA2024-T3 and for the different planes of AA2024-T351 after TCP, all samples being pre-treated with deoxidation 1. For brevity reasons, only the results obtained after 21 days of immersion in 0.5 M NaCl are reported in Fig. 2b. The anticorrosive properties of the TCP coatings were first evaluated by determining the impedance modulus at 10⁻² Hz, referred as $|Z|_{0.01 \text{ Hz}}$, which was considered as a global resistance of the system [10,15]. Results clearly showed that the TCP coated AA2024-T3 exhibited the highest $|Z|_{0.01 \text{ Hz}}$ value ($2.76 \pm 0.01 \cdot 10^6$ Ohm cm²). For the TCP coated AA2024-T351, the $|Z|_{0.01 \text{ Hz}}$ values were lower, but with a higher $|Z|_{0.01 \text{ Hz}}$ value ($1.15 \pm 0.01 \cdot 10^6$ Ohm cm²) for the L/LT_{surface} plane as compared to the L/LT_{core} and LT-ST planes ($0.55 \pm 0.01 \cdot 10^6$ Ohm cm² and $0.70 \pm 0.01 \cdot 10^6$ Ohm cm², respectively). For all samples, a phase signal constituted by two-time constants was observed, related to the

electrochemical processes occurring at the coating/alloy interface, and to the anticorrosion properties of the coating [10,15,25]. However, the shape of the frequency range of high phase angles was different for the LT/ST plane of AA2024-T351, as compared to the other samples. Indeed, for the LT/ST plane of AA2024-T351, the two-time constants were clearly visible, as observed for a bare AA2024 sample [10,15]. For all other samples, visual inspection of the impedance diagrams did not allow to clearly see the two-time constants, but it showed an extension of the measured frequency range of high phase angles. However, the frequency range of high phase angles was significantly larger for AA2024-T3 and the lowest for the L/LT_{core} plane of AA2024-T351. Indeed, the frequency range where the phase angles were under -70° were $2 \cdot 10^2 - 1 \cdot 10^2$ Hz for AA2024-T3, $2 \cdot 10^2 - 1 \cdot 10^1$ Hz for the L-LT_{surface} plane of AA2024-T351 and $3 \cdot 10^1 - 1 \cdot 10^1$ Hz for the L/LT_{core} plane of AA2024-T351. The $|Z|_{0.01 \text{ Hz}}$ values and the frequency range associated with high phase angles could be reported to the anticorrosive properties of the TCP coating as reported by Qi et al. [25]. A high $|Z|_{0.01 \text{ Hz}}$ value could be associated with an improvement of the anticorrosive properties of the TCP coating, which could be attributed to a better adhesion of the coating on the metal or a less defective coating. Moreover, a narrower frequency range with high phase angles ($< -70^\circ$) suggested a decrease of the corrosion resistance of the coating related to an improved penetration of the electrolyte through the defects of the coating [25–27]. Therefore, the results showed that the TCP coating grown on the AA2024-T3 thin sheet had the best protective properties against corrosion. Moreover, it was clearly shown that the sampling direction for the AA2024-T351 thick plate, i.e. the nature of the crystallographic plane, had a significant influence on the anticorrosive properties of the TCP coating with better corrosion resistance for the L/LT_{surface} plane as compared to the L/LT_{core} and LT/ST planes. It could be added here that the results obtained for shorter immersion times led exactly to the same conclusions. For all immersion times in NaCl solution, first, the $|Z|_{0.01 \text{ Hz}}$ values were lower for the AA2024-T351 samples, as compared to AA2024-T3. Moreover, for AA2024-T3, a slight increase of the $|Z|_{0.01 \text{ Hz}}$ values were observed in the 200 first hours, and then the values remained stable. On the contrary, for the AA2024-T351 samples, no increase of the $|Z|_{0.01 \text{ Hz}}$ values, and even a decrease for the L/LT_{core} plane, was observed. The increase in the $|Z|_{0.01 \text{ Hz}}$ values for AA2024-T3 could be explained by referring to a self-healing mechanism helpful in filling the pores and repairing the defects of the TCP coatings, whereas the decrease in $|Z|_{0.01 \text{ Hz}}$ values was related to a degradation of the coating. The results thus suggested more defective TCP coatings for the AA2024-T351 samples, with defects too large to be repaired by a self-healing mechanism. Furthermore, they showed that the deposition of corrosion products that might occur due to the position of the samples in the electrochemical cell did not disturb the results. Results obtained for samples placed vertically in the cell corroborated this hypothesis, with no significant differences observed whatever the position of the samples in the cell.

A comparison between the two deoxidation treatments for the TCP coated AA2024-T3 and the TCP coated LT/ST plane of the AA2024-T351 thick plate was reported in Fig. 2c and d, to check once more whether the differences between AA2024-T3 and AA2024-T351 were observed independently of the pre-treatment. For more brevity, for AA2024-T351, the results are given only for the LT/ST plane that showed the worst corrosion behaviour with deoxidation 1; the results obtained for the other planes of the AA2024-T351 plate are not given, but they did not change the conclusions. Polarisation curves (Fig. 2c) showed a shift of about 60 ± 10 mV for the corrosion potential towards less negative values between deoxidation 1 and deoxidation 2 for the two alloys, but no variation of the pitting potential. Therefore, for both alloys, the potential range corresponding to the passivity plateau was decreased for deoxidation 2 as compared to deoxidation 1 pre-treatment. Moreover, for the thin sheet of AA2024-T3, the corrosion current for the deoxidation 2 pre-treated sample ($3.2 \pm 0.4 \cdot 10^{-9}$ A cm⁻²) was lower than for the deoxidation 1 pre-treated sample ($8.1 \pm 0.5 \cdot 10^{-9}$ A

cm⁻²). On the contrary, for the LT/ST samples of AA2024-T351, the deoxidation 2 pre-treatment led to an increase in the corrosion current with a $3.0 \pm 0.6 \cdot 10^{-6}$ A cm⁻² corrosion current measured after deoxidation 2 by comparison to a value of $4.1 \pm 0.6 \cdot 10^{-8}$ A cm⁻² measured after deoxidation 1 pre-treatment. Taking into account both the variation of the potential ranges corresponding to the passivity and the corrosion current values, it was therefore difficult to conclude about the influence of the deoxidation solution on the anticorrosive properties of the TCP coatings. The main result given from those measurements was that, even with the deoxidation 2 solution, the anticorrosive properties of the TCP coating formed on the AA2024-T351 were lower than those measured for the AA2024-T3 sample. These results were confirmed by impedance measurements. EIS spectra recorded after 21 days in a 0.5 M NaCl solution for the TCP coated AA2024-T3 and AA2024-T351 (LT/ST plane) samples deoxidised with deoxidations 1 and 2 are reported in Fig. 2d. For the AA2024-T3 sample, the frequency ranges of high phase angles were similar with deoxidation solutions 1 and 2 ($2 \cdot 10^2 - 1 \cdot 10^2$ Hz), but the $|Z|_{0.01 \text{ Hz}}$ values were slightly higher for deoxidation 2 ($4.61 \pm 0.01 \cdot 10^6$ Ohm cm²) as compared to deoxidation 1 ($2.76 \pm 0.01 \cdot 10^6$ Ohm cm²). Those results indicated better corrosion resistance for AA2024-T3 pre-treated with deoxidation 2 as compared to deoxidation 1. For the LT/ST plane of the AA2024-T351 thick plate, independent of the pre-treatment, the $|Z|_{0.01 \text{ Hz}}$ values were significantly lower ($0.70 \pm 0.01 \cdot 10^6$ Ohm cm² and $0.26 \pm 0.01 \cdot 10^6$ Ohm cm², for deoxidations 1 and 2, respectively) than those for the TCP coated AA2024-T3 sample, and two time-constants were clearly identified, as for the bare metal, which indicated an important penetration of the electrolyte through the defects of the coating, and therefore, a highly defective coating [10,15]. Therefore, the corrosion properties of the TCP coated AA2024-T351 were significantly lower than those of the TCP coated AA2024-T3, even for the deoxidation 2 solution, in agreement with NSST results and polarisation curves. Moreover, for the LT/ST plane of the AA2024-T351 thick plate, the $|Z|_{0.01 \text{ Hz}}$ value was higher for deoxidation 1 than for deoxidation 2. To strengthen this analysis, the equivalent circuit proposed by Qi et al. (Fig. 3) [27] was used to fit the EIS spectra obtained for both AA2024-T3 and the LT-ST plane of AA2024-T351 samples, for the two deoxidation solutions. As previously done, for brevity, results were only given for LT/ST plane of AA2024-T351 because it presented the worst corrosion behaviour. In agreement with the identification of two time constants, the proposed circuit included i) the electrolyte resistance (R_e), ii) one time constant corresponding to the electrochemical processes at the TCP coating/alloy interface and represented by a parallel combination of the charge transfer resistance R_{ct} and a constant phase element Q_{dl} , and iii) one time constant associated with the conversion coating and represented by the coating resistance R_{coat} and the constant phase element Q_{coat} . Mean values of these parameters are given in Table 2. Results clearly showed that, for all samples, the R_{coat} values were significantly lower than R_{ct} values, which suggested, as previously shown by Qi et al. [27], that the anticorrosive properties of the TCP coating were mainly attributed to the inner layer, with pores and cracks in the TCP coatings allowing access of the electrolyte to the alloy. Therefore, attention was mainly paid to the R_{ct} values; results clearly showed that R_{ct} values were one order of magnitude higher for AA2024-T3 as compared to the LT/ST plane of AA2024-T351, whatever the deoxidation solution. Moreover, considering this parameter, the increase in the corrosion performances for AA2024-T3 with deoxidation 2 solution, as compared to deoxidation 1 solution, was observed, in agreement with NSST results. In the same way, the decrease in the corrosion resistance of AA2024-T351 sample with deoxidation 2 solution, as compared to deoxidation 1, was also confirmed. Fig. 3 showed a comparative analysis of the R_{ct} and $|Z|_{0.01 \text{ Hz}}$ values; the time values corresponding to the formation of the 5th pit during NSST results are also reported. Fig. 3 showed a very good agreement between the three sets of values, which suggested once more a defective structure for the TCP coating formed on the LT/ST plane of AA2024-T351, as compared to AA2024-T3. In

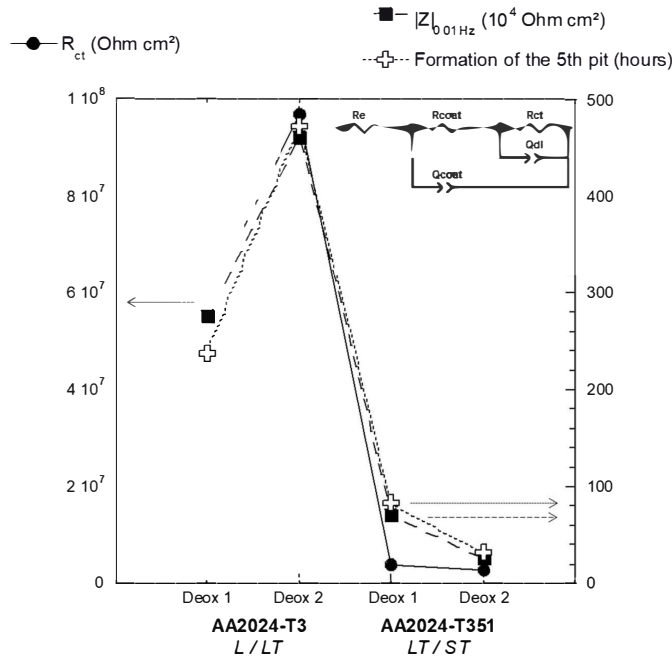


Fig. 3. Evolution of the R_{ct} , $|Z|_{0.01 \text{ Hz}}$ and time of formation of the 5th pit for the AA2024-T3 and the LT/ST plane of AA2024-T351 for two deoxidation solutions. The equivalent circuit used to fit the EIS data is presented here.

Table 2

Parameters extracted from Fig. 2d, i.e., EIS spectra for the different coated samples (AA2024-T3 and LT/ST plane of the AA2024-T351 for the two deoxidation solutions) after 21 days of immersion in 0.5 M NaCl. The equivalent circuit used is presented in Fig. 3.

	2024-T3		2024-T351	
	Deox 1	Deox 2	Deox 1	Deox 2
R_e (ohm cm^2)	60 ± 5	75 ± 5	69 ± 5	64 ± 5
R_{coat} (ohm cm^2)	82 ± 4	38 ± 4	2680 ± 80	1680 ± 60
R_{ct} (ohm cm^2)	$58.30 \cdot 10^6$	$97.02 \cdot 10^6$	$3.84 \cdot 10^6$	$2.85 \cdot 10^6$
Q_{coat} ($\alpha^2/(\text{ohm} \cdot \text{cm}^2)$)	$1.9 \cdot 10^{-6}$	$1.1 \cdot 10^{-6}$	$1.5 \cdot 10^{-6}$	$1.5 \cdot 10^{-6}$
α_{coat}	0.94 ± 0.01	1.00 ± 0.01	0.86 ± 0.01	0.83 ± 0.01
Q_{adl} ($\alpha^2/(\text{ohm} \cdot \text{cm}^2)$)	$2.8 \cdot 10^{-6}$	$4.2 \cdot 10^{-6}$	$2.6 \cdot 10^{-6}$	$15.8 \cdot 10^{-6}$
α_{adl}	0.93 ± 0.01	0.91 ± 0.01	0.86 ± 0.01	0.87 ± 0.01

that sense, the lower values of α_{coat} measured for the LT/ST plane of AA2024-T351 as compared to AA2024-T3, whatever the deoxidation solutions, were in good agreement with this hypothesis. Then, the increase in α_{coat} combined with a decrease in Q_{coat} for AA2024-T3, when deoxidation 2 was compared to deoxidation 1, confirmed the better anticorrosion properties obtained for the deoxidation 2 solution. On the contrary, for the LT/ST plane of AA2024-T351, the decrease in α_{coat} for deoxidation 2 solution, as compared to deoxidation 1, showed the lower anticorrosion properties of the TCP coating formed for the deoxidation 2 solution. Finally, globally, NSST, polarisation tests and EIS experiments led to the same conclusions. Therefore, to go further in the understanding of the differences in corrosion behaviour of the TCP coated AA2024-T3 and AA2024-T351 alloys, the surface Cu coverage of the samples after each step of the pre-treatment, was determined and then analysed taking into account the differences in microstructure between the two alloys.

3.2. Determination of the surface Cu coverage

Many authors attributed the decrease of the anticorrosive properties of the conversion coatings to a surface Cu enrichment during the pre-treatments steps [21,22,28,29]. As indicated in the experimental part, the surface Cu coverage can be determined by CV measurements as shown by Scully et al. [23,24]. Fig. 4a and b compare the surface Cu coverage of the AA2024-T3 and AA2024-T351 (LT/ST plane), respectively, after each step of the surface preparation, for both deoxidation solutions. For comparison, the surface Cu coverage of the as polished surfaces, before the pre-treatment, is also reported (samples are referred as uncoated). For brevity, in Fig. 4a and b, the comparison was made between AA2024-T3 (plane L/LT) and AA2024-T351 with the LT/ST plane only, because this plane presented the worst resistance to corrosion after TCP coating. To complete the results, Fig. 4c reports the results obtained for the three characteristic planes of AA2024-T351, for deoxidation 1 solution. For AA2024-T3, independently of the deoxidation solution, the variation of the surface Cu coverage was similar to that commonly reported in the literature with a significant increase in the surface Cu coverage after degreasing and a significant decrease in this value after deoxidation [15]. The surface Cu coverage of the uncoated samples was attributed to the response of mainly S-phase IMCs. During degreasing, S-phase IMCs could dissolve leading to Cu redeposition [10], so that, after degreasing, the surface Cu coverage could be attributed to both S-phase IMCs and Cu deposits [30,31]. After deoxidation with the deoxidation 1 solution, SEM-FEG observations showed that the major part of the S-phase IMCs was removed for AA2024-T3, with a fraction of surface area covered by S-phase IMCs decreasing from 0.8 % for uncoated samples to 0.3 % after degreasing and deoxidation (considering only the S-phase IMCs with a diameter higher than 1 μm); therefore, the surface Cu coverage after degreasing and deoxidation was attributed mainly to Cu deposits, which showed that the Cu deposits had been only partially removed during deoxidation [30]. Results also showed that, for the sample deoxidized with deoxidation 2, the surface Cu coverage was higher after degreasing:

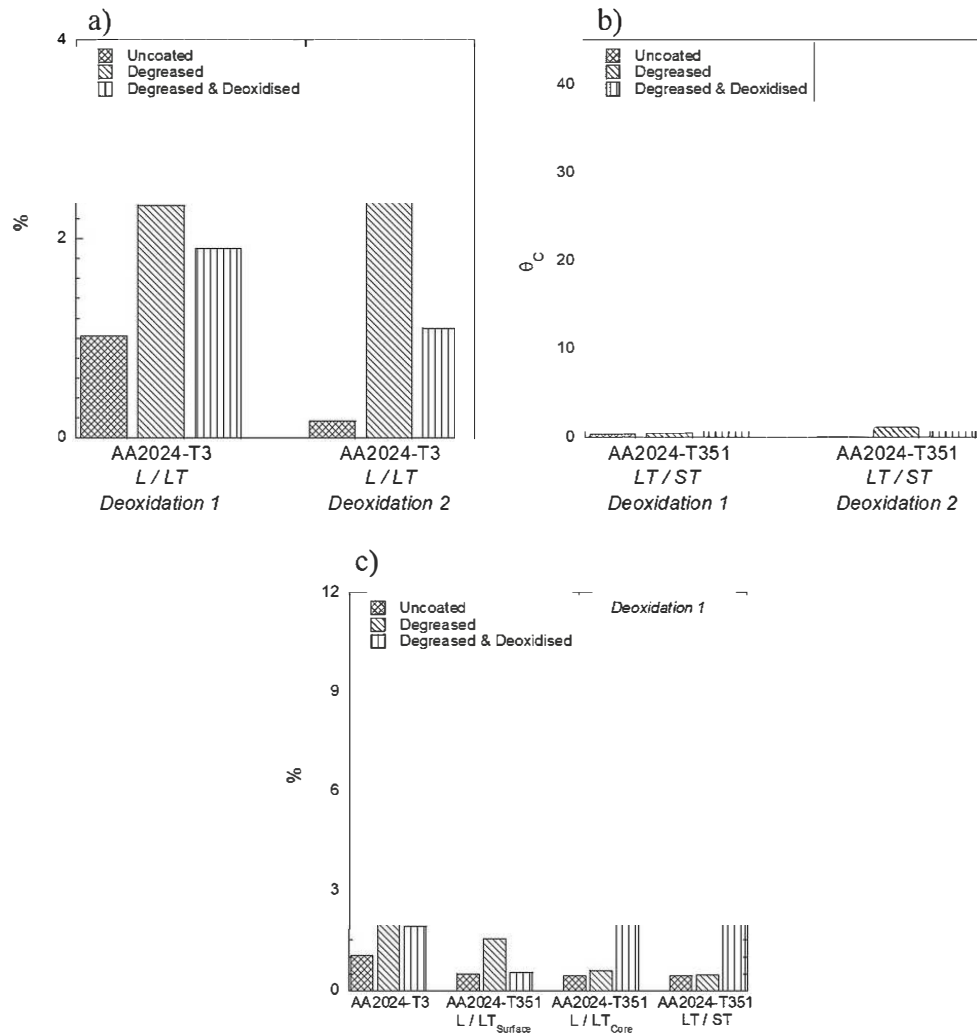


Fig. 4. Surface Cu coverage measured for uncoated, degreased and degreased & deoxidised samples. a) AA2024-T3 (L/LT), deoxidation 1 and 2 solutions, b) AA2024-T351 (LT/ST), deoxidation 1 and 2 solutions, and c) AA2024-T3 (L/LT) and AA2024-T351 (L/LT_{surface}, L/LT_{core} and LT/ST), deoxidation 1 solution.

taking into account that the degreasing step was similar as for deoxidation 1 sample, such variation in the surface Cu coverage could be attributed to the intrinsic variation in reactivity of the S-phase IMCs [32,33]. After deoxidation with the deoxidation 2 solution, a slightly lower surface Cu coverage (1.1 ± 0.3 %) was measured compared to that measured with the deoxidation 1 solution (1.9 ± 0.3 %). SEM-FEG observations of the degreased and deoxidized surface showed that, after degreasing and deoxidation with deoxidation 2 solution, the fraction of surface area covered by S-phase IMCs was lower than 0.1 %, as compared to 0.3 % for the sample deoxidized with deoxidation 1 solution, which could explain the differences in the surface Cu coverage. Moreover, it was of interest to note that the lower surface Cu coverage measured for deoxidation 2 sample, compared to deoxidation 1 sample, could be related to its better corrosion behaviour determined by corrosion tests above. However, again, the main result was the highly significant difference in behaviour measured for the AA2024-T351 (LT/

ST plane) sample as compared to AA2024-T3. Indeed, for AA2024-T351 (LT/ST plane), whatever the deoxidation solution, the surface Cu coverage was also found to increase after degreasing, as for the AA2024-T3, but, after deoxidation, it went on increasing, reaching 10 ± 1 % for deoxidation 1 and 40 ± 2 % for deoxidation 2. It was of major interest to note here that the differences in surface Cu coverage values between AA2024-T3 and AA2024-T351 samples were highly significant. Similar results were obtained by Viroulaud et al. [21] for AA2024-T351. The authors showed by using X-ray photoelectron spectroscopy an increase in the surface Cu coverage after deoxidation using a sulfo-nitro-ferric solution; moreover, by performing ToF-SIMS analyses, they showed that, after degreasing, Cu was mainly localised on the S-phase intermetallics, whereas, after deoxidation, it was distributed all over the surface, probably due to a strong redeposition process. However, Fig. 4c shows that the variation in the surface Cu coverage as a function of the pre-treatment steps, was dependent on the nature of the plane for

AA2024-T351. Indeed, a similar behaviour was observed for LT/ST and L/LT_{core} planes of the AA2024-T351 thick plate, whereas, the variation in surface Cu coverage for the L/LT_{surface} plane of AA2024-T351 was similar to that observed for the AA2024-T3 sample. Those differences suggested that the reactivity of S-phase IMCs was dependent on the characteristic plane considered for AA2024-T351, or that other microstructural parameters had to be taken into account and contributed also to explain the surface Cu coverage values. Nevertheless, as shown above for AA2024-T3, a relationship between the surface Cu coverage after the pre-treatment and the anticorrosive properties of the TCP coatings could be established, in agreement with literature [15]. Firstly, the high surface Cu coverage measured for the AA2024-T351 samples (LT/ST and L/LT_{core} planes) could be related to the lower anticorrosive properties measured for the TCP coatings formed on these samples compared to both the TCP coated AA2024-T3 and L/LT_{surface} plane of AA2024-T351 thick plate. Then, the higher surface Cu coverage measured for the LT/ST plane of AA2024-T351 for deoxidation 2 solution, as compared to deoxidation 1 solution, could be related also to the lower corrosion resistance measured for the sample deoxidised with deoxidation 2 solution, as shown by NSST but also impedance measurements. To better understand such a relationship, the morphology of the TCP coatings was studied, considering both the surface Cu enrichment and the roughness of the TCP coating / alloy interface, but also the thickness and homogeneity of the TCP coating.

3.3. Analysis of the morphology of the TCP coatings: thickness and homogeneity, roughness of the TCP coating / alloy interface and Cu enrichment

SEM-FEG micrographs of cross-sections of TCP coatings formed on AA2024-T3 and AA2024-T351 (plane LT/ST), for both deoxidation 1 and deoxidation 2 solutions, are reported in Fig. 5. For all samples, the post-treatment PACS generated a particular morphology at the TCP coating surface characterised by rare earth element-rich lamellar particles (shown by the black arrows), with a similar size for both deoxidation solutions [34]. Under this lamellar-structured layer, the TCP coatings appeared more or less homogeneous for all samples. For deoxidation 1 solution, the TCP coating thickness was about 110 nm for both AA2024-T3 and AA2024-T351 (the vertical scale is different from

the horizontal scale due to the tilt for SEM-FEG observations). By comparison to deoxidation 1, with deoxidation 2 solution, the thickness of the TCP coating increased significantly (about 145 nm) for AA2024-T3, whereas it decreased significantly for the LT/ST plane of AA2024-T351 (about 80 nm). Comparison with the results obtained for the anticorrosive properties (Figs. 1–3) showed that there was not a trivial thickness / anticorrosive properties of the TCP coating relationship. In particular, the lower anticorrosive properties of the TCP coating formed on AA2024-T351, for deoxidation 1 solution, compared to AA2024-T3, could not be explained only by considering the thickness of the TCP coatings. Results clearly showed that other parameters had to be taken into account. Fig. 5 also showed that, for both deoxidation solutions, the adherence of the TCP coatings on the alloys was better for AA2024-T3 than for AA2024-T351. It is important to note here that all FIB preparations were done in a similar way. Even though some artifacts cannot be completely avoided due to FIB preparation, there was no reason to have more artifacts for AA2024-T351 as compared to AA2024-T3. Therefore, observations clearly showed a stronger detachment of the TCP coating formed on AA2024-T351 as compared to AA2024-T3, even though it was difficult to quantify this phenomenon because artifacts due to the FIB preparation could not be completely avoided. Moreover, independently of the deoxidation solution, for AA2024-T351 samples, a well-marked white layer was observed at the TCP coating / alloy interface; it was less visible for AA2024-T3. Local EDS analyses showed that it was a Cu layer. To confirm the identification of this white layer, cross-sections of the TCP coatings were observed by TEM, and EDS maps were plotted. Figs. 6 and 7 show the TEM observations and associated Zr, Cr and Cu maps for the coated AA2024-T3 and AA2024-T351 samples, respectively (for deoxidation 2 solution). Results allowed to identify a Cu-rich layer at the interface TCP coating / alloy for both AA2024-T3 and AA2024-T351 samples (shown by the white arrows in Figs. 6d and 7d, respectively). Moreover, GDOES analyses confirmed a Cu enrichment at this interface for both AA2024-T3 (Fig. 6e) and AA2024-T351 (Fig. 7e). Finally, Cu maps, obtained in the same conditions for the two alloys, clearly showed that the Cu-rich layer was more visible for AA2024-T351, as compared to AA2024-T3, in agreement with the higher surface Cu coverage measured for AA2024-T351 (Fig. 4). Viroulaud showed that the kinetics of TCP coating growth depended on the surface Cu coverage: a high

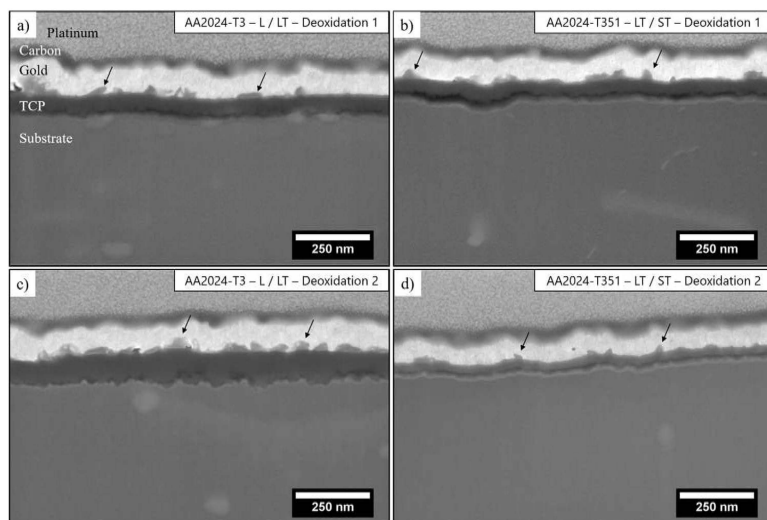


Fig. 5. SEM-FEG observations of cross-sections obtained for TCP coated AA2024 samples. a) AA2024-T3 (L/LT) and b) AA2024-T351 (LT/ST) for deoxidation 1 solution; c) AA2024-T3 (L/LT) and d) AA2024-T351 (LT/ST) for deoxidation 2 solution.

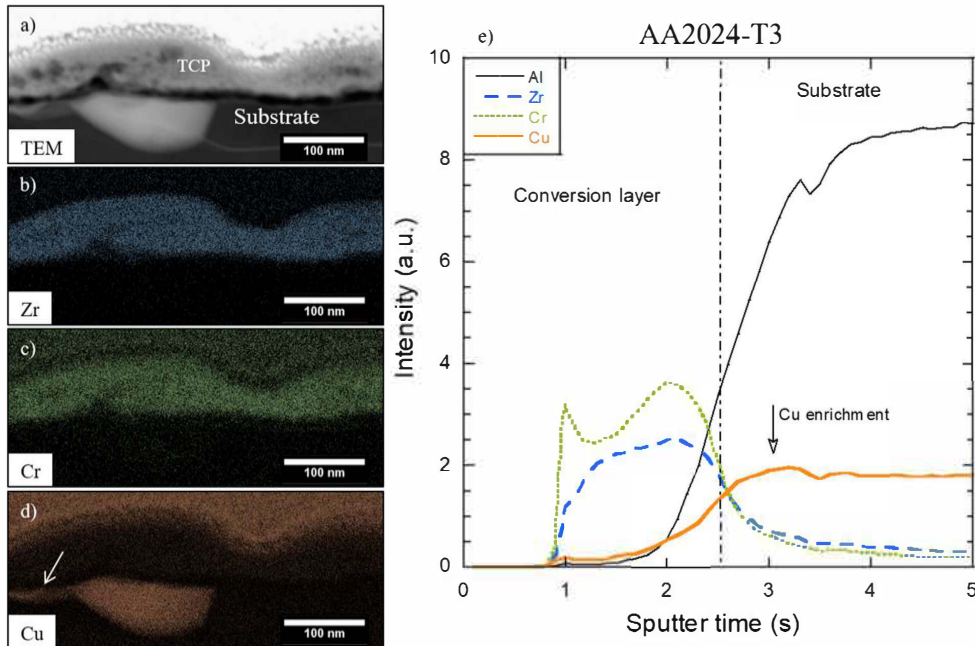


Fig. 6. a) TEM images and b),c) and d) TEM-EDS maps (Zr, Cr and Cu, respectively) of the TCP coating formed on AA2024-T3. e) GD-OES profiles of Al, Zr, Cr and Cu for the TCP coated AA2024-T3.

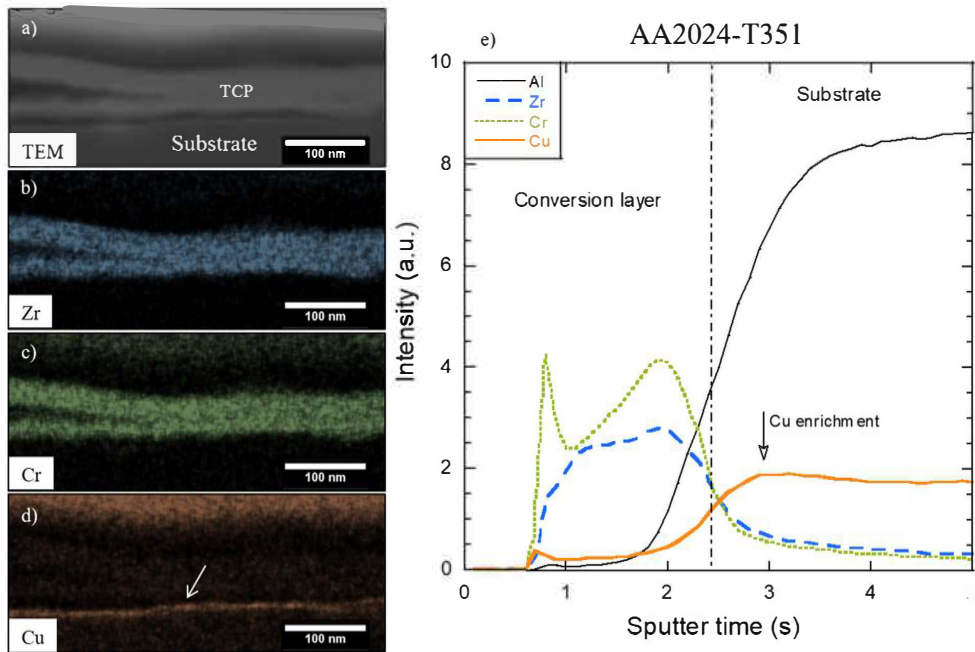


Fig. 7. a) TEM images and b),c) and d) TEM-EDS maps (Zr, Cr and Cu, respectively) of the TCP coating formed on the LT/ST plane of the AA2024-T351. e) GD-OES profiles of Al, Zr, Cr and Cu for the TCP coated LT/ST plane of the AA2024-T351.

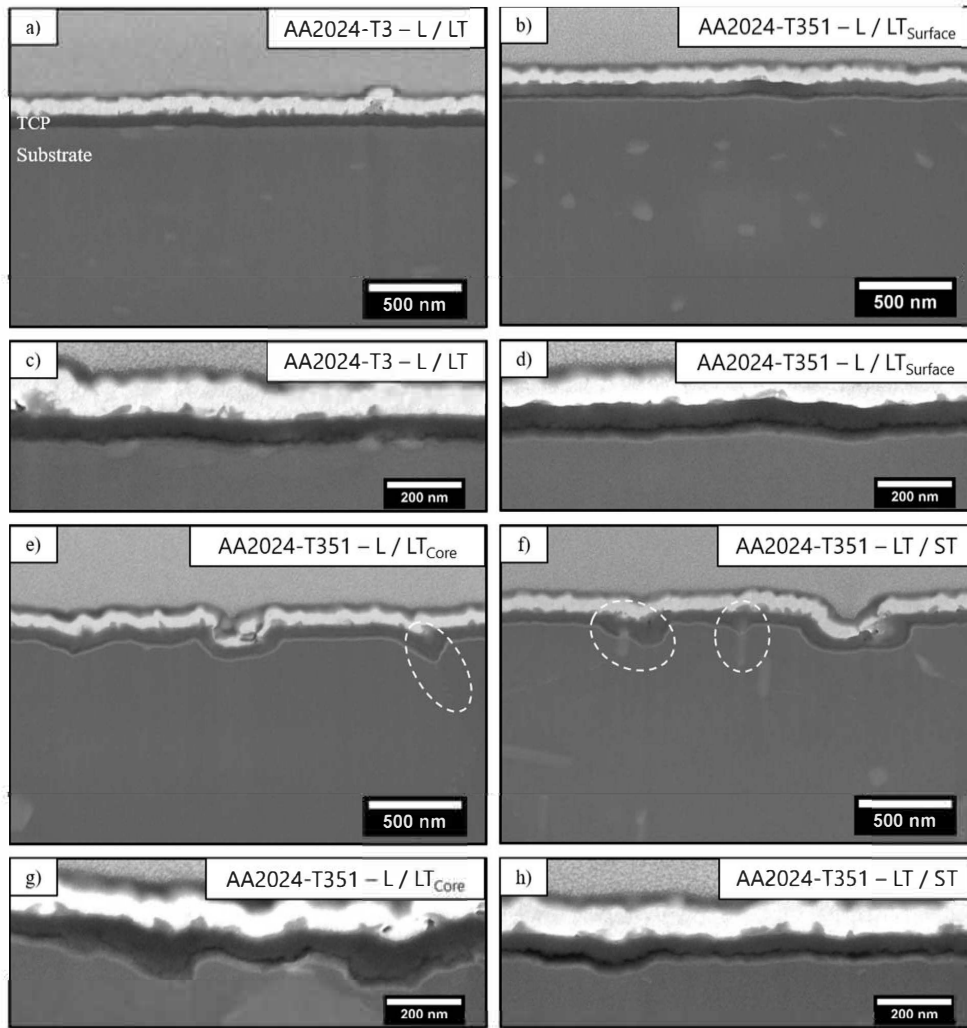


Fig. 8. SEM-FEG observations of cross-sections obtained for TCP coated AA2024 samples. a) AA2024-T3 (L/LT), b) AA2024-T351 (L/LT_{surface}), c) close-up for a), d) close-up for b), e) AA2024-T351 (L/LT_{core}), f) AA2024-T351 (LT/ST), g) close-up for e), h) close-up for f). Deoxidation was performed with deoxidation 1 solution.

surface Cu coverage could be associated with a fast kinetics of coating growth, which could lead to thicker TCP coatings, but it could be mainly related to more defective coatings with lower anticorrosive properties [21]. Such an approach would be helpful to explain the anticorrosive properties determined before, with results leading to an impossibility to establish a clear relationship between the thickness of the TCP coatings and their anticorrosive properties. Furthermore, it could be useful also to understand the relationship between the surface Cu coverage and the morphology of the TCP coating, considering that a high surface Cu coverage could be either associated with a thick TCP coating and/or defective (e.g., delaminated, cracked) coating. In order to go further with this analysis, cross-sections of the TCP coatings formed on the different planes of AA2024-T351 were observed by using SEM-FEG, for deoxidation 1 solution (Fig. 8). Observations for AA2024-T3 are reported for comparison. An accurate observation of the TCP coating / alloy interface for all samples showed that i) locally, the TCP

coating could be thicker for AA2024-T351 samples, in particular for L/LT_{core} and LT/ST planes, ii) the roughness of the interface was higher and the adherence of the TCP coating to the substrate was lower for L/LT_{core} and LT/ST planes of AA2024-T351, and iii) the Cu layer was well-marked for AA2024-T351 samples and much less visible for AA2024-T3. Therefore, results clearly showed that a high surface Cu coverage was most often associated with detachment of the coating from the substrate. Moreover, the local increase in the thickness of the TCP coating for AA2024-T351 samples (L/LT_{core} and LT/ST planes) could be related to high local Cu concentration. An accurate observation of Fig. 8e and f showed that the zones where the TCP coating was locally thicker were often associated with the presence of Cu-rich particles identified as Cu-rich intergranular precipitates (circles in Fig. 8e) or Al-Cu-Mn dispersoids (circles in Fig. 8f). Those observations strongly suggested the influence of Cu on the kinetics of coating growth. Furthermore, they also suggested that the surface Cu coverage had to be

explained probably considering the reactivity of both the intragranular Cu-rich IMCs, but also that of the Cu-rich solid solution, in relation with the presence of Cu-rich dispersoids, and of the Cu-rich intergranular precipitates, when present in the material, as previously said. This was discussed later in the manuscript (paragraph 3.4.). Finally, the observation of more defective TCP coatings, i.e. less homogeneous in thickness and less adherent to the substrate, for both L/LT_{core} and LT/ST planes of AA2024-T351, was relevant considering the lower corrosion resistance measured for those samples (Figs. 1 and 2), and confirmed that the anticorrosive properties of the TCP coatings could not be explained by considering their thickness only. The results were therefore in agreement with literature, Cu acting as a catalytic agent and generating many defects in TCP coatings [15,21,22,29,35]. This might be explained by considering that a strong kinetics of coating growth should generate internal stresses leading either to the formation of cracks or to the detachment of the coating from the surface. In the last case, the TCP coating should stop growing, after having begun growing faster. This should explain why very thick TCP coatings were not observed systematically on surfaces with a high surface Cu coverage.

3.4. Identification of the critical microstructural parameters

The results shown above clearly demonstrated that the morphology and anticorrosive properties of the TCP coatings formed on AA2024 samples could be explained, at least partially, considering the surface Cu coverage measured after the pre-treatment step. Literature showed that the Cu deposits observed after the pre-treatment can be related to the reactivity of S-phase IMCs [36]. As previously said, in the present study, SEM-FEG observations confirmed the reactivity of S-phase IMCs, with the surface area covered by S-phase IMCs in AA2024-T3, that decreased from 0.8 % for uncoated samples to 0.3 % and 0.1 % after degreasing followed by deoxidation 1 and deoxidation 2 solutions, respectively. Therefore, after the pre-treatment, the major part of S-phase IMCs was dissolved for AA2024-T3 for deoxidation 2 solution (Fig. 9a), leading to Cu redeposition, and then to an increase in the surface Cu coverage as compared to uncoated samples. The results are not shown for deoxidation 1 solution but they were similar. However, for AA2024-T351, independently of the metallurgical planes, results showed significant differences in the reactivity of S-phase IMCs. For deoxidation 1 solution, the major part of S-phase IMCs (fraction of surface area covered by these particles in uncoated samples of about 0.8 %, as for AA2024-T3) was dissolved also (not shown), but, for deoxidation 2 solution, the reactivity of S-phase IMCs led to the presence of Cu-rich sponges after degreasing and deoxidation (Fig. 9b). Such a difference in the reactivity of the S-phase IMCs between the two alloys could be explained firstly considering their size: for AA2024-T3, the mean surface area covered by one S-phase IMC, i.e. the mean size of one particle, was $2.4 \mu\text{m}^2$, whereas it was $44 \mu\text{m}^2$ for AA2024-T351, which was probably due to the fragmentation of S-phase IMCs during the cold-

rolling pass for AA2024-T3. Wang et al. clearly showed that there was an influence of the particle size on their reactivity and the dissolution of the matrix around [37]. However, it is true that the study performed by these authors was focused on small particles. Therefore, the most relevant explanations could be found referring to the work of Parvizi et al., who showed that dislocation structures were observed around the IMCs; during exposure to an aggressive solution, those structures acted as pathways for corrosive species and led to enhanced local dissolution processes [38,39]. The dislocation structures were clearly dependent on the IMC size; in that way, the IMC size could affect the electrochemical processes that occurred at the IMCs sites. Concerning now the differences observed depending on the deoxidation solutions, what could be thought is that the fragmented particles of AA2024-T3 are small enough to be easily removed during pre-treatments, whatever the deoxidation solution, as shown before with surface area covered by the IMCs after pre-treatments of 0.3 % and 0.1 % for deoxidation 1 and deoxidation 2 solutions, respectively. Therefore, the Cu deposition related to the IMCs was globally similar whatever the deoxidation solution. This suggested that other microstructural parameters had to be considered to explain the slight difference in surface Cu coverage measured after the pre-treatments for AA2024-T3. The difference in the dissolution rate of the matrix (50 nm min^{-1} and 0.2 nm min^{-1} for deoxidation 1 and 2, respectively) could explain the lower Cu surface coverage for deoxidation 2, which could be also related to the increase in corrosion performances measured for deoxidation 2 as compared to deoxidation 1. Nevertheless, it can be remembered here that the difference in surface Cu coverage was small, from 1.1 ± 0.3 to 1.9 ± 0.3 % after deoxidations 2 and 1, respectively, which could also explain that no significant differences in corrosion performances were observed between deoxidations 1 and 2 by using polarisation curves. For AA2024-T351, significant differences were observed concerning the dissolution of the IMCs as indicated before. Those differences could be also linked to the aggressivity of the two deoxidation solutions, with a lower etching speed for deoxidation 2 as compared to deoxidation 1, that could be significant here because of the larger size of the IMCs in AA2024-T351 as compared to AA2024-T3. After deoxidation 2, the Cu-rich sponges observed for AA2024-T351 (Fig. 9b) probably contributed significantly to the high surface Cu coverage measured after the pre-treatment step (Fig. 4), as shown by Qi et al. [36]. This could be related to the decrease in corrosion performances measured for AA2024-T351 after deoxidation 2 as compared to deoxidation 1.

However, as indicated previously, the relationship between the surface Cu coverage, the thickness of the TCP coating, and finally its anticorrosive properties was not trivial. Indeed, after deoxidation 1 treatment, the global thickness of the TCP coatings formed on AA2024-T3 and the LT/ST plane of AA2024-T351 was similar (Fig. 5b), whereas the surface Cu coverage was significantly higher and the corrosion performances lower for AA2024-T351 as compared to AA2024-T3. After deoxidation 2, the TCP coating formed on the LT/ST plane of AA2024-T351 was less thick, despite of a significantly higher surface Cu

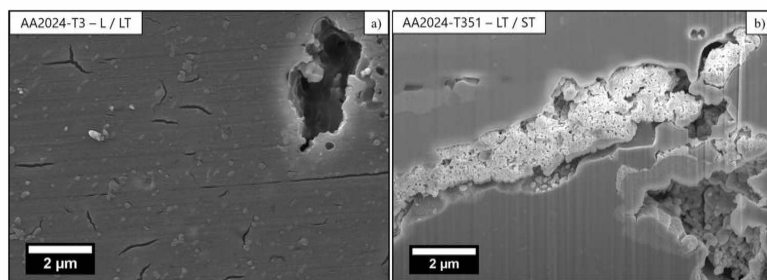


Fig. 9. SEM-FEG observations of AA2024 samples after degreasing and deoxidation (deoxidation 2 solution). a) AA2024-T3 sample. b) AA2024-T351 (LT/ST) sample.

coverage, and showed lower anticorrosion properties. This led us to assume that the dealloying of S-phase particles was not the only parameter that contributed to the surface Cu coverage; this was in agreement with the previous comments about the dissolution of the matrix. Then, it could be assumed also, as previously indicated, that Cu mainly influenced the kinetics of coating growth [21], which could be not directly linked to the final thickness: with a high kinetics of coating growth, the internal stresses in the TCP coating could become strong enough to lead to a detachment of the coating from the surface, and thus the coating growth stopped [25]. Furthermore, this would be associated with a defective structure of the TCP coating. Such an approach should be in perfect agreement with the clear relationship between the surface Cu coverage and the anticorrosive performances of the TCP coatings. Therefore, to strengthen this assertion, attention was paid again to the structure of the TCP coatings and identification of other microstructural parameters to explain the surface Cu coverage values and defective structure of the TCP coating formed on both L/LT_{core} and LT/ST planes of AA2024-T351.

As previously noticed in Fig. 8f, local increase of the TCP coating, associated with a detachment of the coating from the substrate, was also observed where Cu-rich dispersoids were found: galvanic coupling between those dispersoids and the matrix in the TCP solutions probably led to increased dissolution of the matrix and then to higher local Cu deposition explaining the local thickness of the TCP coating [37]. Furthermore, Fig. 10b also showed that the TCP coating formed on AA2024-T351 (LT/ST plane), for a deoxidation 1 solution, exhibited a

defective structure at the grain boundaries, which was observed, neither for this alloy treated with deoxidation 2 solution, nor for AA2024-T3 alloy (Fig. 10a and c). An accurate observation of the TCP coatings for AA2024-T351, for deoxidation 1 solution, clearly showed that the thickness of the coating formed at the grain boundaries was different by comparison to that formed on the matrix. Two types of observations could be done: in Fig. 10e, a local increase in the TCP coating thickness was observed at a grain boundary, whereas, in Fig. 10f, cracking of the TCP coating was observed, even if a very local penetration of the TCP coating inside the metal was observed just below the crack (close-up in Fig. 10f). Moreover, the defective structure of the TCP coatings at the grain boundaries became more and more marked from the L/LT_{surface} plane, L-LT_{core} plane to LT/ST plane (Fig. 10d, e and f). Therefore, significant differences in the TCP coating morphology were observed depending on the planes considered for the AA2024-T351 alloy. This was also true in the early stages of the TCP coating growth, for deoxidation 1 solution (Fig. 11). After 3 s of immersion in the TCS solution, for all samples, the TCP coating was clearly visible at the sample surface with nodules covering the whole surface, even though some large holes attributed to the removing of S-phase IMCs were observed [40]. For AA2024-T3 (Fig. 11a) and the L/LT_{surface} plane (Fig. 11b) of AA2024-T351, no other defect was observed, whereas, for the L/LT_{core} (Fig. 11c) and LT/ST (Fig. 11d) planes of AA2024-T351 samples, a breakdown was clearly observed at the grain boundaries. This defective structure of the TCP coating at the grain boundaries of AA2024-T351 samples could be associated with the reactivity of Cu-rich intergranular precipitates.

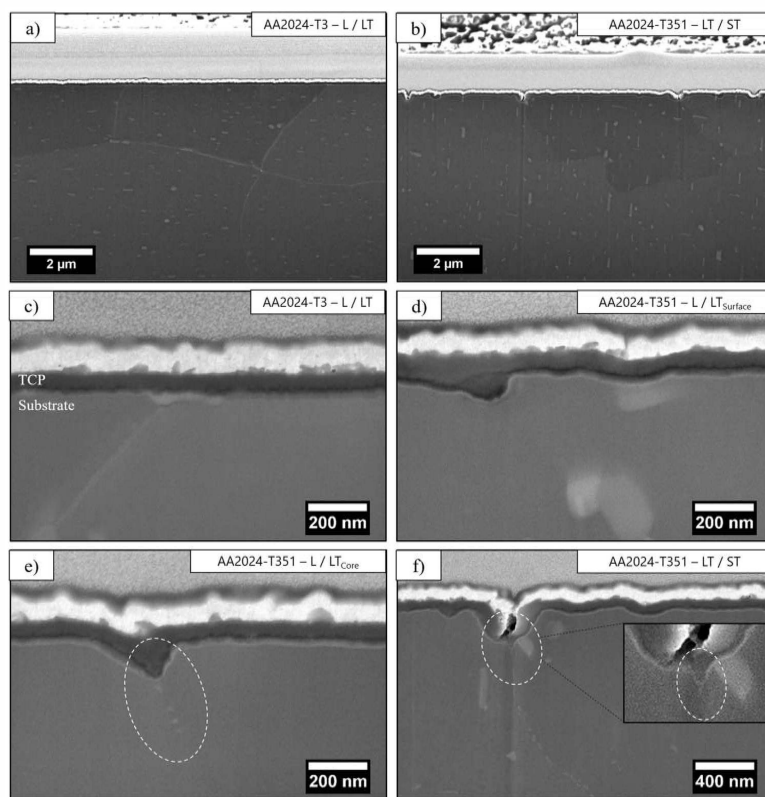


Fig. 10. SEM-FEG observations of cross-sections of TCP coated AA2024 samples (deoxidation was performed with deoxidation 1 solution). a) AA2024-T3 (L/LT), b) AA2024-T351 (LT/ST), c) close-up for a), d) AA2024-T351 (L/LT_{surface}), e) AA2024-T351 (L/LT_{core}), f) close-up for b).

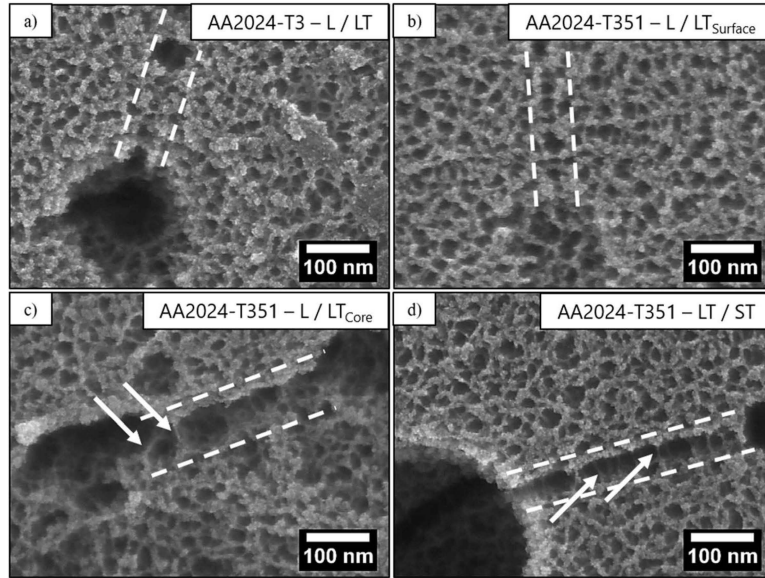


Fig. 11. SEM-FEG surface observations of AA2024 samples degreased, deoxidised (deoxidation 1 solution) and immersed in the TCS bath for 3 s. a) AA2024-T3 (L/LT), b) AA2024-T351 (L/LT_{surface}), c) AA2024-T351 (L/LT_{core}), d) AA2024-T351 (LT/ST). The dashed lines indicate the grain boundaries.

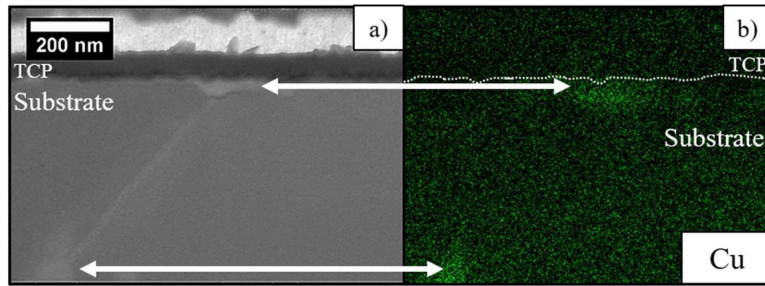


Fig. 12. a) SEM-FEG observation of a cross section of TCP coated AA2024-T3 sample b) Cu EDS map of the same zone as in a).

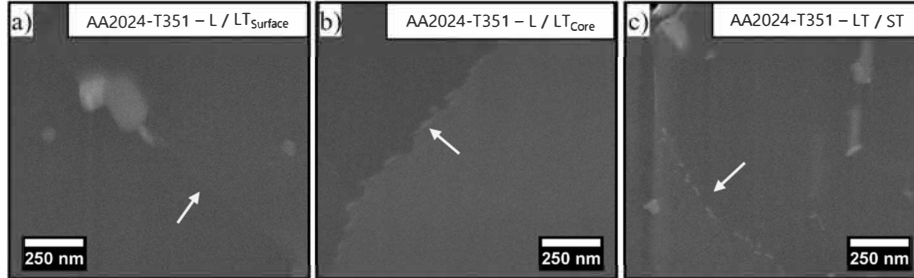


Fig. 13. SEM-FEG observations of AA2024-T351 samples after polishing a) L/LT_{surface}, b) L/LT_{core} and c) LT/ST planes. Arrows show Cu-rich intergranular precipitates.

Indeed, SEM-FEG observations of a cross-section of the TCP coating formed on AA2024-T3 (Figs. 10c and 12a) revealed the presence of white spots at some grain boundaries under the TCP coating. EDS analysis showed that this white spot was Cu deposit (Fig. 12b),

probably linked to the dealloying of Cu-rich intergranular precipitates. It could be noted here that, due to the size of the Cu deposits, a contribution of other microstructural parameters, e.g. the matrix that dissolved during the pre-treatment, was to be considered. Fig. 13 showed

SEM-FEG observations of AA2024-T351 (all metallurgical planes) samples. For the L/LT_{surface} plane, only a few Cu-rich intergranular precipitates (Fig. 13a) were visible, whereas, for the L/LT_{core} and LT/ST planes, more numerous and larger Cu-rich intergranular precipitates were observed (Fig. 13b and c), as previously noticed in Figs. 8 and 10. For the AA2024-T3 sample, SEM-FEG observations did not allow to detect intergranular precipitates, but transmission electron microscopy (TEM) observations (not shown here) revealed the presence of some rare and fine Cu-rich intergranular precipitates at some grain boundaries. Such a distribution of the Cu-rich intergranular precipitates, depending on the metallurgical state of the alloy, was in agreement with literature [14]. For AA2024-T3 and the L/LT_{surface} plane of AA2024-T351, the quenching rate was too fast to allow the precipitation of a large amount of Cu-rich precipitates at the grain boundaries. On the contrary, for the L/LT_{core} and LT/ST planes of AA2024-T351, the quenching rate was slower due to the thickness of the plate, so that numerous and bigger Cu-rich precipitates could be observed. Figs. 10 and 11 showed that the dealloying of those precipitates occurred during the pre-treatment leading to a Cu-enrichment at the grain boundaries, which could influence the TCP coating growth. For AA2024-T3, considering the low amount of Cu-rich intergranular precipitates, no defective structure of the TCP coating was observed at the grain boundaries, so that the Cu-enrichment remained visible after the TCP coating growth (Fig. 12). It was nearly similar for the L/LT_{surface} plane of AA2024-T351, where the defective structure of the TCP coating at the grain boundaries was not well-marked (Fig. 10d). On the contrary, for both L/LT_{core} and LT/ST planes of AA2024-T351, the amount of Cu-rich intergranular precipitates was enough to significantly influence the local Cu content, and consequently the TCP coating growth: a very defective structure was observed so that the Cu-rich deposits were not observed any more. In this analysis, it was assumed that the local Cu enrichment linked to the dealloying of the Cu-rich intergranular precipitates led, as explained before, to an increase in the kinetics of the coating growth. This was in agreement with observations of Fig. 10e. Moreover, it could be confirmed that, when the coating was too thick, a crack could form as shown in Fig. 10f; nevertheless, due to the presence of other Cu-rich intergranular precipitates, new local penetrations of the TCP coating were then observed below the crack (close-up in Fig. 10f). Going back to Fig. 11c and d, the breakdown of the TCP coating at some grain boundaries of the L/LT_{core} and LT/ST planes of AA2024-T351 could be related to either very reactive grain boundaries for which cracks were observed very rapidly, or to grain boundaries where the dealloying of Cu-rich intergranular precipitates had just begun. In any cases, those observations could be explained by considering the differences in reactivity of the grain boundaries depending on different parameters [41]; they also confirmed the major contribution of the grain boundaries to the defective structure of the TCP coatings formed on the L/LT_{core} and LT/ST planes of AA2024-T351.

Finally, it was of major interest to note that several metallurgical parameters contributed to explain the defective structure of the TCP coatings formed on AA2024-T351, depending on the metallurgical plane. However, their contribution to this defective structure depended, in particular, on the deoxidation solution. For deoxidation 2 solution, as said above, no dealloying of the Cu-rich intergranular precipitates was observed for AA2024-T351. In that case, the anticorrosive properties of the TCP coating formed on AA2024-T351 were mainly linked to the reactivity of S-phase IMCs during the pre-treatment. For deoxidation 1 solution, no Cu-rich sponge was observed for the AA2024-T351 samples, whereas numerous defects were observed at the grain boundaries: in that case, the defects at the grain boundaries played a major role on the anticorrosive properties of the TCP coatings formed on AA2024-T351. Other parameters had also to be considered, e.g. the presence of Cu-rich dispersoids, the reactivity of the Cu-rich matrix. Globally, the contribution of all parameters to the decrease in anticorrosive properties of the TCP coatings depended both on the nature of the deoxidation solution and on the metallurgical state of AA2024.

4. Conclusions

The main conclusions of this work can be summarised as follows:

- 1 For the two deoxidation solutions tested, the anticorrosive properties of the TCP coating formed on AA2024-T3 were better than for AA2024-T351. For this last alloy, the TCP coated L/LT_{surface} plane has a better corrosion resistance than the L/LT_{core} and LT/ST planes.
- 2 A clear relationship between the surface Cu coverage measured after the pre-treatment (degreasing and deoxidation) and the anticorrosive properties of the TCP coatings was established. Cu was shown to lead to an increase in the kinetics of coating growth, which could be associated to internal stresses inside the coating and subsequent detachment of the coating from the substrate.
- 3 The differences in surface Cu coverage between the different samples, and therefore the differences in anticorrosive properties of the TCP coatings, are explained by i) a different reactivity of S-phase IMCs in the deoxidation solution, due to their differences in size between AA2024-T3 and AA2024-T351, and probably also due to the level of misorientation of the surrounding matrix (dislocations structures), and by ii) the presence of more numerous and bigger intergranular Cu-rich precipitates in L/LT_{core} and LT/ST planes for AA2024-T351 as compared to the L/LT_{surface} plane of AA2024-T351 and AA2024-T3.
- 4 The reactivity of both S-phase IMCs and intergranular Cu-rich precipitates was dependent on the deoxidation solution, so that the contribution of the S-phase IMCs and Cu-rich intergranular precipitates to the anticorrosive properties of the TCP coatings varied significantly depending on the deoxidation solution. The contribution of the matrix dissolution, associated with the presence of Cu-rich dispersoids, could not be neglected.

From an industrial point of view, the results clearly showed that, depending on the metallurgical state of AA2024, the process for the TCP coating growth had to be adapted.

Data availability

The raw/processed data required to reproduce these findings cannot be shared at this time as the data also forms part of an ongoing study.

Author statement

X. Verdalet-Guardiola: Investigations. Formal analysis. Validation. Visualization. Methodology. Data curation. Writing-original draft. Writing-Review & Editing.

R. Saillard: Investigations. Formal analysis. Validation. Visualization. Methodology. Data curation. Writing-original draft. Writing-Review & Editing.

B. Fori: Funding acquisition (financial support). Resources (Materials). Project administration. Writing-Review & Editing.

S. Duluard: Funding acquisition. Methodology. Project administration. Supervision. Validation. Conceptualization. Data curation. Writing-Review & Editing.

C. Blanc: Funding acquisition. Methodology. Project administration. Supervision. Validation. Conceptualization. Data curation. Writing-original draft. Writing-Review & Editing.

Declaration of Competing Interest

The authors declare that they have no known competing financial interests or personal relationships that could have appeared to influence the work reported in this paper.

Acknowledgements

This work was performed in the framework of the NEPAL FUI project. CIRIMAT was financially supported by the French Ministry of Economy and industry (BPI-France), the Région Occitanie/Pyrénées-Méditerranée and the European Union (FEDER/ERDF). The authors thank also Mecaprotec and the ANRT for their financial support (Xavier Verdalet-Guardiola's PhD thesis). Finally, they thank Claudie Josse (platform of Micro-characterisation Raimond Castaing, Toulouse, France) for the FIB cutting.

Appendix A. Supplementary data

Supplementary material related to this article can be found, in the online version, at doi:<https://doi.org/10.1016/j.corsci.2020.108508>.

References

- [1] A.S.M. International, A.I.H. Committee, A.I.A.P.D. Committee, Properties and Selection, ASM International, 1990.
- [2] T. Muster, A.E. Hughes, G.E. Thompson, Copper Distribution in Al Alloys, Nova Science Publishers, 2007.
- [3] A.E. Hughes, G.E. Thompson, J.M. Mol, N. Birbilis, S.J. Garcia, X. Zhou, High Strength Al-Alloys: Microstructure, Corrosion and Principles of Protection, INTECH Open Access Publisher, 2011.
- [4] A.E. Hughes, A. Boag, A.M. Glenn, D. McCulloch, T.H. Muster, C. Ryan, C. Luo, X. Zhou, G.E. Thompson, Corrosion of AA2024-T3 part II: co-operative corrosion, Corros. Sci. 53 (2011) 27–39, <https://doi.org/10.1016/j.corsci.2010.09.030>.
- [5] European Chemical Agency, REACh Annex XIV, (2013).
- [6] C. Matzdorf, M. Kane, J. Green, Corrosion Resistant Coatings for Aluminum and Aluminum Alloys, US6375726B1, (2002) (accessed December 26, 2018), <https://patents.google.com/patent/US6375726/it>.
- [7] P. Bares, C. Stephan, C. Gazeau, Method for the Surface Treatment of Parts Made of an Aluminium or Magnesium Alloy, WO2013117767A1, (2013) (accessed December 26, 2018), <https://patents.google.com/patent/WO2013117767A1/en>.
- [8] Y. Guo, G.S. Frankel, Characterization of trivalent chromium process coating on AA2024-T3, Surf. Coat. Technol. 206 (2012) 3895–3902, <https://doi.org/10.1016/j.surfcoat.2012.03.046>.
- [9] C. Cai, X.-Q. Liu, X. Tan, G.-D. Li, H. Wang, J.-M. Li, J.-F. Li, A Zr- and Cr(III)-containing conversion coating on Al alloy 2024-T3 and its self-repairing behavior, Mater. Corros. 68 (2017) 338–346, <https://doi.org/10.1002/maco.201609067>.
- [10] X. Verdalet-Guardiola, J.-P. Bonino, S. Duluard, B. Fori, C. Blanc, Influence of the alloy microstructure and surface state on the protective properties of trivalent chromium coatings grown on a 2024 aluminium alloy, Surf. Coat. Technol. 344 (2018) 276–287, <https://doi.org/10.1016/j.surfcoat.2018.03.046>.
- [11] G. Acosta, L. Veleza, D. de la Fuente, Mapping the initial corrosion activity of aluminium alloy 2024-T3 in diluted substitute ocean water by localized electrochemical impedance spectroscopy, Mater. Corros. 69 (2018) 1368–1374, <https://doi.org/10.1002/maco.201810109>.
- [12] A. Boag, A.E. Hughes, N.C. Wilson, A. Torpy, C.M. MacRae, A.M. Glenn, T.H. Muster, How complex is the microstructure of AA2024-T3? Corros. Sci. 51 (2009) 1565–1568, <https://doi.org/10.1016/j.corsci.2009.05.001>.
- [13] A.E. Hughes, A.M. Glenn, N. Wilson, A. Moffatt, A.J. Morton, R.G. Buchheit, A consistent description of intermetallic particle composition: an analysis of ten batches of AA2024-T3, Surf. Interface Anal. 45 (2013) 1558–1563, <https://doi.org/10.1002/sia.5207>.
- [14] M.-L. de Bonfils-Lahovary, L. Laffont, C. Blanc, Characterization of intergranular corrosion defects in a 2024 T351 aluminium alloy, Corros. Sci. 119 (2017) 60–67, <https://doi.org/10.1016/j.corsci.2017.02.020>.
- [15] R. Saillard, B. Viguier, G. Odemer, A. Pugliara, B. Fori, C. Blanc, Influence of the microstructure on the corrosion behaviour of 2024 aluminium alloy coated with a trivalent chromium conversion layer, Corros. Sci. 142 (2018) 119–132, <https://doi.org/10.1016/j.corsci.2018.07.007>.
- [16] J.E. Hatch, Aluminum—Properties and Physical Metallurgy, ASM International, Materials Park, Ohio, 1984.
- [17] C. Blanc, B. Lavelle, G. Mankowski, The role of precipitates enriched with copper on the susceptibility to pitting corrosion of the 2024 aluminium alloy, Corros. Sci. 39 (1997) 495–510.
- [18] A. Korchev, A. Kahoul, Corrosion behavior of commercial aluminum alloy processed by equal channel angular pressing, Int. J. Corros. (2013) 1–11, <https://doi.org/10.1155/2013/983261>.
- [19] C. Xu, R. Zheng, S. Hanada, W. Xiao, C. Ma, Effect of hot extrusion and subsequent T6 treatment on the microstructure evolution and tensile properties of an Al-6Si-2Cu-0.5Mg alloy, Mater. Sci. Eng. A 710 (2018) 102–110, <https://doi.org/10.1016/j.msea.2017.10.052>.
- [20] N. Wint, Z.S. Barrett, G. Williams, H.N. McMurray, The study of AA2024 de-alloying using luminol electrogenerated chemiluminescence imaging, J. Electrochem. Soc. 166 (2019) C3417–C3430, <https://doi.org/10.1149/2.0481911jes>.
- [21] R. Viroulaud, J. Świątowska, A. Seyeux, S. Zanna, J. Tardelli, P. Marcus, Influence of surface pretreatments on the quality of trivalent chromium process coatings on aluminum alloy, Appl. Surf. Sci. 423 (2017) 927–938, <https://doi.org/10.1016/j.apsusc.2017.06.246>.
- [22] J. Qi, Y. Miao, Z. Wang, Y. Li, X. Zhang, P. Skeldon, G.E. Thompson, Influence of copper on trivalent chromium conversion coating formation on aluminum, J. Electrochem. Soc. 164 (2017) C611–C617.
- [23] M.A. Jakab, D.A. Little, J.R. Scully, Experimental and modeling studies of the oxygen reduction reaction on AA2024-T3, J. Electrochem. Soc. 152 (2005) B311–B320, <https://doi.org/10.1149/1.1949047>.
- [24] D.A. Little, M.A. Jakab, J.R. Scully, Effect of surface pretreatment on the underpaint corrosion of AA2024-T3 at various temperatures, Corrosion 62 (2006) 300–315, <https://doi.org/10.5006/1.3280663>.
- [25] J. Qi, T. Hashimoto, J. Walton, X. Zhou, P. Skeldon, G.E. Thompson, Formation of a trivalent chromium conversion coating on AA2024-T351 alloy, J. Electrochem. Soc. 163 (2016) C25–C35.
- [26] C.A. Matzdorf, W.C. Nickerson, E. Lipnickas, Evaluation of modified zirconium/trivalent chromium conversion coatings by accelerated corrosion and electrochemical techniques, Tri-Serv. Corros. Conf. NACE International, Orlando, Florida, U.S.A, 2005, pp. 1–22.
- [27] J.-T. Qi, T. Hashimoto, J.R. Walton, X. Zhou, P. Skeldon, G.E. Thompson, Trivalent chromium conversion coating formation on aluminium, Surf. Coat. Technol. 280 (2015) 317–329.
- [28] A.J. Davenport, R.G. Bin, Copper accumulation during cleaning of Al-Cu alloys, Corros. Corros. Prev. Low Density Met. Alloys Proc. Int. Symp. (2001) 41–46.
- [29] Q. Meng, G.S. Frankel, Effect of copper content on chromate conversion coating protection of 7xxx-T6 aluminum alloys, Corrosion 60 (2004) 897–905, <https://doi.org/10.5006/1.3287823>.
- [30] A.J. Davenport, B. Liu, Copper accumulation during cleaning of Al-Cu alloys, Electrochemical Society Proceedings (2001) 41–46.
- [31] T. Hashimoto, X. Zhang, X. Zhou, P. Skeldon, S.J. Haigh, G.E. Thompson, Investigation of dealloying of S phase (Al₂CuMg) in AA 2024-T3 aluminium alloy using high resolution 2D and 3D electron imaging, Corros. Sci. 103 (2016) 157–164.
- [32] A. Boag, A.E. Hughes, A.M. Glenn, T.H. Muster, D. McCulloch, Corrosion of AA2024-T3 part I: localised corrosion of isolated IM particles, Corros. Sci. 53 (2011) 17–26, <https://doi.org/10.1016/j.corsci.2010.09.009>.
- [33] X. Zhou, C. Luo, T. Hashimoto, A.E. Hughes, G.E. Thompson, Study of localized corrosion in AA2024 aluminium alloy using electron tomography, Corros. Sci. 58 (2012) 299–306, <https://doi.org/10.1016/j.corsci.2012.02.001>.
- [34] A.-I. Stoica, J. Świątowska, A. Romaine, F. Di Franco, J. Qi, D. Mercier, A. Seyeux, S. Zanna, P. Marcus, Influence of post-treatment time of trivalent chromium protection coating on aluminium alloy 2024-T3 on improved corrosion resistance, Surf. Coat. Technol. 369 (15) (2019) 186–197, <https://doi.org/10.1016/j.surfcoat.2019.04.051>.
- [35] S.J. Garcia-Vergara, K. El Khazmi, P. Skeldon, G.E. Thompson, Influence of copper on the morphology of porous anodic alumina, Corros. Sci. 48 (2006) 2937–2946, <https://doi.org/10.1016/j.corsci.2005.10.017>.
- [36] J. Qi, A. Němcová, J.R. Walton, X. Zhou, P. Skeldon, G.E. Thompson, Influence of pre- and post-treatments on formation of a trivalent chromium conversion coating on AA2024 alloy, Thin Solid Films 616 (2016) 270–278, <https://doi.org/10.1016/j.tsf.2016.08.044>.
- [37] J. Wang, B. Zhang, B. Wu, X.L. Ma, Size-dependent role of S phase in pitting initiation of 2024Al alloy, Corros. Sci. 105 (2016) 183–189, <https://doi.org/10.1016/j.corsci.2016.01.016>.
- [38] R. Parvizi, A.E. Hughes, M.Y. Tan, R.K.W. Marceau, M. Forsyth, P. Cizek, A.M. Glenn, Probing corrosion initiation at interfacial nanostructures of AA2024-T3, Corros. Sci. 116 (2017) 98–109, <https://doi.org/10.1016/j.corsci.2016.12.006>.
- [39] R. Parvizia, A.E. Hughes, A.M. Glenn, P. Cizek, M.Y. Tan, M. Forsyth, Role of microstructure in corrosion initiation of a highly-deformed AA2024 wire, Corros. Sci. 144 (2018) 184–197, <https://doi.org/10.1016/j.corsci.2018.08.052>.
- [40] X. Verdalet-Guardiola, B. Fori, J.-P. Bonino, S. Duluard, C. Blanc, Nucleation and growth mechanisms of trivalent chromium conversion coatings on 2024-T3 aluminium alloy, Corros. Sci. 155 (2019) 109–120, <https://doi.org/10.1016/j.corsci.2019.04.035>.
- [41] M. Guérin, J. Alexis, E. Andrieu, L. Laffont, W. Lefebvre, G. Odemer, C. Blanc, Identification of the metallurgical parameters explaining the corrosion susceptibility in a 2050 aluminium alloy, Corros. Sci. 102 (2016) 291–300, <https://doi.org/10.1016/j.corsci.2015.10.020>.